# C3N5: A Low Bandgap Semiconductor Containing an Azo-Linked Carbon Nitride Framework for Photocatalytic, Photovoltaic and Adsorbent Applications

Pawan Kumar,*,[†] Ehsan Vahidzadeh,[†] Ujwal K. Thakur,[†] Piyush Kar,[†] Kazi M. Alam,[†] Ankur Goswami,[†] Najia Mahdi,[†] Kai Cui,[‡] Guy M. Bernard,[§] Vladimir K. Michaelis,[§] and Karthik Shankar*,[†]

[†]Department of Electrical and Computer Engineering, University of Alberta, 9211 116 Street, Edmonton, Alberta T6G 1H9, Canada
[‡]Nanotechnology Research Centre, National Research Council of Canada, Edmonton, Alberta T6G 2M9, Canada
[§]Department of Chemistry, University of Alberta, Edmonton, Alberta T6G 2G2, Canada

**S** Supporting Information

**ABSTRACT:** Modification of carbon nitride based polymeric 2D materials for tailoring their optical, electronic and chemical properties for various applications has gained significant interest. The present report demonstrates the synthesis of a novel modified carbon nitride framework with a remarkable 3:5 C:N stoichiometry ($C_3N_5$) and an electronic bandgap of 1.76 eV, by thermal deammoniation of the melem hydrazine precursor. Characterization revealed that in the $C_3N_5$ polymer, two s-heptazine units are bridged together with azo linkage, which constitutes an entirely new and different bonding fashion from $g-C_3N_4$ where three heptazine units are linked together with tertiary nitrogen. Extended conjugation due to overlap of azo nitrogens and increased electron density



on heptazine nucleus due to the aromatic $\pi$ network of heptazine units lead to an upward shift of the valence band maximum resulting in bandgap reduction down to 1.76 eV. XRD, He-ion imaging, HR-TEM, EELS, PL, fluorescence lifetime imaging, Raman, FTIR, TGA, KPFM, XPS, NMR and EPR clearly show that the properties of $C_3N_5$ are distinct from pristine carbon nitride ($g-C_3N_4$). When used as an electron transport layer (ETL) in $MAPbBr_3$ based halide perovskite solar cells, $C_3N_5$ outperformed $g-C_3N_4$, in particular generating an open circuit photovoltage as high as 1.3 V, while $C_3N_5$ blended with $MA_xFA_{1−x}Pb(I_{0.85}Br_{0.15})_3$ perovskite active layer achieved a photoconversion efficiency (PCE) up to 16.7%. $C_3N_5$ was also shown to be an effective visible light sensitizer for $TiO_2$ photoanodes in photoelectrochemical water splitting. Because of its electron-rich character, the $C_3N_5$ material displayed instantaneous adsorption of methylene blue from aqueous solution reaching complete equilibrium within 10 min, which is significantly faster than pristine $g-C_3N_4$ and other carbon based materials. $C_3N_5$ coupled with plasmonic silver nanocubes promotes plasmon-exciton coinduced surface catalytic reactions reaching completion at much low laser intensity (1.0 mW) than $g-C_3N_4$, which showed sluggish performance even at high laser power (10.0 mW). The relatively narrow bandgap and 2D structure of $C_3N_5$ make it an interesting air-stable and temperature-resistant semiconductor for optoelectronic applications while its electron-rich character and intrasheet cavity make it an attractive supramolecular adsorbent for environmental applications.
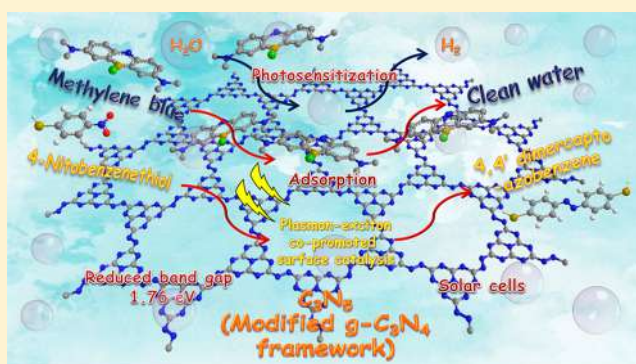
## INTRODUCTION

The last few decades have witnessed the rise of semiconducting, all-organic polymers as excellent metal-free and visible light-active materials for various optoelectronic and energy harvesting applications.[1] Although impressive improvements in performance have been achieved, particularly for plastic solar cells, the synthesis procedures for semiconducting polymers are cumbersome and difficult to scale up,[2] and the organic semiconductors themselves are unstable under the action of heat, light and/or ambient air.[3] Consequently, there are scalability concerns related to semiconducting polymers,[4]

and requirement of heavy encapsulation to achieve even modest durability in the photovoltaic application. The same concerns, related to oxidative stability and durability, have also ruled out the use of semiconducting polymers in photocatalytic applications.

A very different approach toward forming and exploiting all-organic, polymeric semiconductors in optoelectronic and energy harvesting applications consists of using doped and

substituted graphenic frameworks as building blocks to achieve two-dimensional (2D) semiconductors with well-defined bandgaps and structural motifs.[5,6] The major advantages of graphenic semiconductors are their chemical robustness and the simplicity of synthesis. Several graphenic semiconductors are synthesizable using solvothermal synthesis and/or solid-state reactions, and graphenic semiconductors are perfectly stable in ambient conditions up to temperatures of several hundred degrees Celsius. As a result of this exceptional stability, almost no structural or chemical degradation of photocatalytic action is observed even after several reuse cycles.[7]

Among graphenic semiconductors, graphitic carbon nitride (g-$C_3N_4$), composed of tris-s-triazine (s-heptazine, $C_6N_7$) units bridged together with nitrogen atoms to give a 2D graphitic structure has gained significant interest due to its astonishing electronic, optical and physicochemical properties.[8] Continuous repetition of the heptazine motif leads to a bandgap of 2.7 eV with band edge positions ($E_{CB}$, −1.1 eV and $E_{VB}$, +1.6 eV) that render it compatible with sunlight-driven water splitting, $CO_2$ photoreduction and the photooxidation of a number of organic compounds.[9] Further, the plentiful presence of electron-rich sites and basic nitrogens in the g-$C_3N_4$ scaffold enables the promotion of various catalytic reactions, i.e., alkylation, esterification, oxidation, etc. and pollutant removal (dye adsorption).[6a,10] The somewhat wide bandgap of g-$C_3N_4$ means that it can absorb only the ultraviolet and blue fraction of the solar spectrum ($\lambda < 450$ nm), which limits its performance in photocatalytic and photovoltaic applications. Doping with various heteroatoms such as P, F, B and S has been utilized to improve the visible light absorption profile and photoefficiency.[11] Like all semiconductors, g-$C_3N_4$ suffers the innate drawback of carrier recombination, detrimental to catalytic and photocatalytic processes. Many surface modification approaches such as increasing the surface area via soft and hard templating, using two or more precursors, transformation of bulk material into sheets, doping with metals (Ag, Cu, Rh, Pt, Na, etc.) and metal oxides ($CoO_x$) for electron and hole capture, coupling with other semiconductors/metal complexes to form heterojunctions, and blending with graphene have been employed to improve the photocatalytic and catalytic performance of g-$C_3N_4$.[12] However, less attention has been paid to chemical structure modification, which can lead to the generation of a more robust, band edge tuned g-$C_3N_4$ framework with entirely new physicochemical properties for efficient catalytic/photocatalytic applications. It has been found that addition of extra nitrogen-rich moieties in the g-$C_3N_4$ scaffold to increase the N:C ratio from 4:3 ratio in carbon nitride (CN) can reduce the bandgap significantly, due to a more extended conjugated network and the participation of the lone pair on the N atom with the $\pi$ conjugated system of heptazine motif. Vinu et al. demonstrated the synthesis of N-rich carbon nitride (MCN-8) using 3-amino-1,2,4-triazole to afford $C_3N_5$ stoichiometry resulting in a significant decrease in bandgap (2.2 eV) due to extended conjugation.[13] However, this increase in N:C ratio to 5:3 (from the 4:3 ratio in g-$C_3N_4$) was due to the presence of the N-rich 1,2,4-triazole moiety linked to the heptazine motif and not because of the direct incorporation of the extra N atom in the heptazine nucleus. The same group has also reported the synthesis of mono/and diamino-s-tetrazine based carbon nitride materials (i.e., MCN-ATN, MCN-4 and MCN-9) with $C_3N_5$ to $C_3N_6$ stoichiometry using 3-amino-1,2,4-triazine/aminoguanidine hydrochloride

precursor and SBA-15/KIT-6 templating material.[14] The N-rich 1,2,4-triazine or 1,2,4,5-tetrazine moieties were bridged together with tertiary nitrogen in a similar fashion to triazine based carbon nitride and a significant decrease in band gap was observed due to the addition of extra nitrogens. In a recent report, mesoporous triazole and triazine framework modified carbon nitride materials with $C_3N_{4.8}$ empirical formula was synthesized by using 5-amino-1H-tetrazole (5-ATTZ) precursor and their hybrid with graphene displayed excellent performance in the oxygen reduction reaction.[15] Fang et al. reported the synthesis of nitrogen self-doped graphitic carbon nitride ($C_3N_{4+x}$) by heating hydrazine treated melamine in a sealed ampule. In $C_3N_{4+x}$, the excess N atoms replace terminal C atoms in the heptazine nucleus and the excess charge on the N atom gets redistributed leading to electron-rich heptazine motifs due to which $C_3N_{4+x}$ possessed a narrower bandgap (2.65 eV) with concomitant shifts in the conduction and valence band edge positions ($E_{CB}$, −0.98 eV and $E_{VB}$, +1.67 eV).[16] In these N-rich carbon nitrides, the N-rich triazine or heptazine based unit remains linked together with tertiary nitrogen, $N(C)_3$ and increased stochiometric N:C ratio was due to the replacement of C via N in triazine or heptazine ring system. Similarly, carbon-rich $C_3N_4$ network also facilitates bandgap narrowing and efficient charge separation due to the extended conjugated network. Zhang et al. reported the hydrothermal synthesis of low bandgap, C-rich $C_3N_4$ materials with extended conjugated networks using melamine (as heptazine ring source) and glucose (as carbon source) precursors.[17] However, the use of melamine and other C and N sources can afford only $C_3N_4$ structures possessing randomly distributed domains within the $C_3N_4$ framework due to the uncontrolled reaction and these regions work as trap centers. Melem (2,5,8-triamino-s-heptazine) considered the smallest monomeric unit of g-$C_3N_4$ framework, provides the opportunity to manipulate chemical structure by incorporating other units in the $C_3N_4$ framework in a more controlled fashion.[16−18] Shiraishi et al. reported the synthesis of modified CN-polydiimide framework (g-$C_3N_4$/$PDI_x$) by solid-state reaction between melem and electron deficient pyromellitic dianhydride (PMDA) and demonstrated that the band edge positions of g-$C_3N_4$/$PDI_x$ could be tuned by limiting the number of PDI units in the framework.[19] Heterostructured ($C_{ring}$-$C_3N_4$) embodiments of conductive, in-plane, $\pi$ conjugated carbon rings incorporated in the $C_3N_4$ matrix were prepared by thermal dehydrogenation reaction between glucose and melem, and the obtained $C_{ring}$-$C_3N_4$ heterostructure achieved fast spatial charge transfer from g-$C_3N_4$ to $C_{ring}$ motif facilitating efficient water splitting.[20] The replacement of amino functionalities on melem/melamine by nitrogen-rich functionalities, i.e., azide (−$N_3$), expedited the synthesis of N-rich carbon nitride, i.e., 2,5,8-triazido-s-heptazine, ($C_6N_7$)-($N_3$)$_3$, which after thermal heating, afforded N-rich carbon nitride.[21] Likewise, triazine containing N-rich CN was also synthesized by thermal annealing of 2,4,6-triazido-1,3,5-triazine [cyanuric triazide, ($C_3N_3$)($N_3$)$_3$].[22] However, the synthesis procedure involved sodium azide and concomitant shock sensitive explosion hazards; furthermore, azide intermediates are highly undesirable.

Herein, we demonstrated the synthesis of a novel modified carbon nitride framework with a $C_3N_5$ stoichiometry by thermal deammoniation of 2,5,8-trihydrazino-s-heptazine, also known as melem hydrazine (MH), as a safe and environmentally benign precursor (Figure 1). The obtained carbon
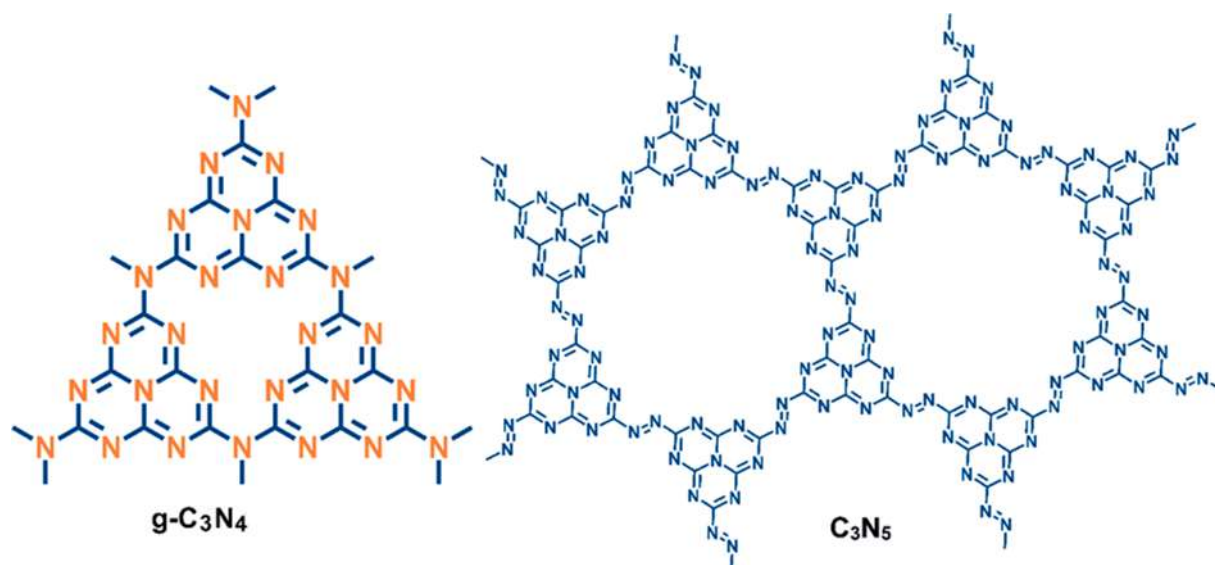
**Figure 1.** Chemical structure of g-$C_3N_4$ and carbon nitride modified $C_3N_5$ framework.
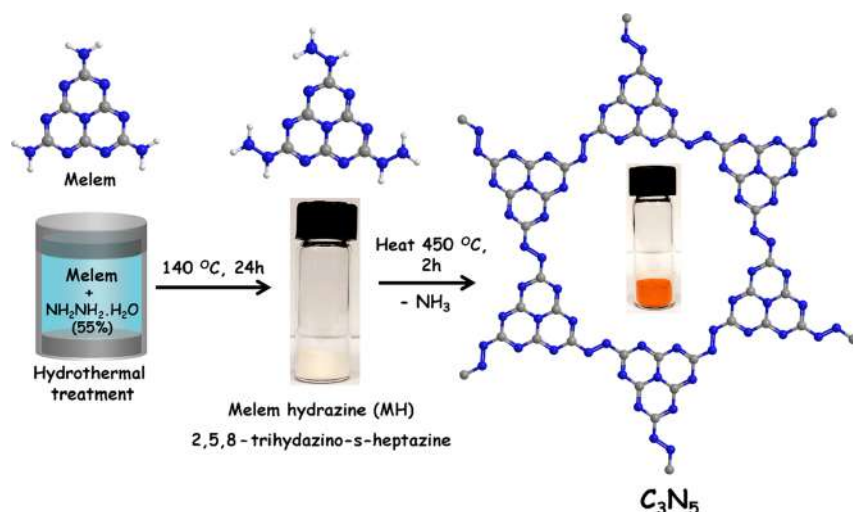


**Figure 2.** Synthesis schematic of $C_3N_5$ from melem via melem hydrazine (Atom color: N - blue, C - gray and H - white). The vials show the distinct color of the reaction product contrasted with that of the precursor.

nitride modified framework was denoted as $C_3N_5$ due to its 3:5 C:N stoichiometric ratio. Characterization studies revealed that the $C_3N_5$ framework contains heptazine moieties bridged together by azo linkage (−N=N−). The presence of azo linkage extends the $\pi$ conjugated network due to overlap between the $p$ orbitals on N atoms constituting the azo bond and $\pi$ system of heptazine motif, which resulted in the reduction of the electronic bandgap to 1.76 eV. $C_3N_5$ displayed improved photosensitization properties at longer wavelengths for solar water splitting. Further, because of the increased electron charge density on the ring nitrogen, $C_3N_5$ exhibited instantaneous adsorption of methylene blue from aqueous solution. Solar cell devices fabricated using low bandgap $C_3N_5$, as an electron transporting layer (ETL) in MAPbBr$_3$ based perovskite solar cells demonstrated improved power conversion efficiency (PCE), open circuit voltage ($V_{oc}$) etc. compared to solar cells made from g-$C_3N_4$ based ETL due to tuned band alignment. Blending a small amount of $C_3N_5$ (4.0 wt %) with MA$_x$FA$_{1−x}$Pb(I$_{0.85}$Br$_{0.15}$)$_3$ perovskite active layer led to an increase in PCE up to 16.68% with $V_{oc}$ of 1.065 V and $J_{sc}$

of 22.87 mA/cm$^2$ higher than conventional and g-$C_3N_4$ blended solar cell architectures. Compared to g-$C_3N_4$, $C_3N_5$ exhibited a remarkably enhanced performance in the plasmon-exciton codriven photoreduction of 4-nitrobenzenethiol to 4,4′-dimercaptoazobenzene.

## ■ RESULTS AND DISCUSSION

Melem (2,5,8-triamino-$s$-heptazine) served as the precursor monomeric unit for the synthesis of $C_3N_5$ polymer. Melem was synthesized by heating melamine at 425 °C overnight followed by purification in boiling water. The obtained melem was treated with hydrazine hydrate (NH$_2$NH$_2$·H$_2$O, 55% in water) in an autoclave at 140 °C for 24 h. The treatment of melem with hydrazine hydrate transformed amino (−NH$_2$) functionalities into hydrazino (−NH−NH$_2$) functionalities, which afforded melem hydrazine, MH (2,5,8-trihydrazino-$s$-heptazine).[23,24] The obtained white melem hydrazine was subjected to programmed heating at 450 °C for 2 h to obtain orange colored $C_3N_5$ polymer (Figure 2) (see Supporting Information for experimental details). Melem hydrazine has a highly

hydrogen bonded structure which facilitates the formation of an azo-bridged heptazine framework by thermal condensation. Previously, Gillan also reported the formation of similar azo-bridged functionalities by heating nitrogen-rich 2,4,6-cyanuric triazide or triazido-1,3,5-triazine $(C_3N_3)(N_3)_3$ to form differential composition triazine based carbon nitride.[22] In the same report, Gillan suggested that transformation of cyanuric triazide into azo-bridged triazine carbon nitride framework proceeded through the nitrene intermediate $(C_3(N_3)_2N:)$ and that the formation of $C_3N_5$ from melem hydrazine might proceed via a similar intermediate due to the thermolabile nature of hydrazine functionalities. The structures of melem, melem hydrazine and hydrogen bonded melem hydrazine are given in Supporting Information (Figure S1).

The surface morphology of the $C_3N_5$ polymer was investigated using a He-ion microscope equipped with an electron flood gun to facilitate positive charge neutralization accumulated from the He-ion beam (Figure 3a). The He-ion
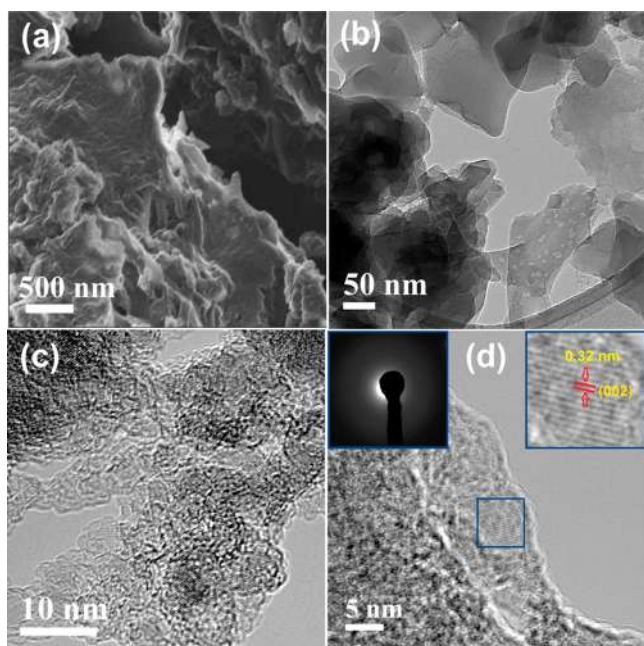


**Figure 3.** (a) He-ion image of $C_3N_5$, and HR-TEM images of $C_3N_5$ (b) at 50 nm, (c) at 10 nm and (d) at 5 nm scale bar; left and right insets showing SAED diffraction pattern and interplanar $d$ spacing, respectively.

images of MHP show a rough, crumpled graphenic scaffold with some erupted morphologies, which indicate that the high temperature treatment of MH monomeric unit facilitated polymerization into an irregular sheet-like structure. The fine structure of $C_3N_5$ material was determined using high resolution transmission electron microscopy (HR-TEM) (Figure 3b–d). The carbon nitride like layered sheet architecture is clearly evident in the TEM image of $C_3N_5$ at 50 nm scale bar (Figure 3b). Under long duration exposure of the electron beam, $C_3N_5$ starts to degrade and shrink which likely resulted due to high energy electrons breaking the $-N=N-$ linkage. HR-TEM images at 10 and 5 nm scale bar show crystallite fringes of nanoporous multilayered sheets with an interplanar $d$-spacing of 0.32 nm, corresponding to the 002 plane of the graphitic structure (Figure 3c,d, and inset). The observed $d$-spacing in $C_3N_5$ was identical to g-$C_3N_4$ from

which we infer that during the thermal polymerization step, the stacking pattern of sheets in $C_3N_5$ remains similar to that in bulk g-$C_3N_4$. The broad, less intense ring in the selected area electron diffraction (SAED) pattern was attributed to diffraction of electrons by the 002 plane; however, the low intensity of the ring suggests amorphous nature of the material (inset of Figure 3d).

The surface chemical composition of the synthesized material was investigated using X-ray photoelectron spectroscopy, XPS (Figure 4). The XPS elemental survey scan of $C_3N_5$ shows peaks corresponding to C 1s, N 1s, Na 1s, Cl 2p and O 1s (Figure S2a). The presence of Na 1s and Cl 2p is due to intercalated Na$^+$ ions in the supramolecular cavity of the polymeric motif (Figure 1) and the residual NaCl formed during the purification step of MH. After excluding Na 1s, Cl 2p and O 1s peaks, the at. % values of C and N in the $C_3N_5$ were found to be 36.76% and 63.24% respectively, which represent an empirical formula of $C_3N_{5.16}$ for the $C_3N_5$ polymer (Table 1). The obtained composition matched well with theoretical $C_3N_5$ (C - 37.50 at. %, and N - 62.50 at. %) stoichiometric carbon nitride materials. The high resolution XPS spectrum of $C_3N_5$ in C 1s region was deconvolved into two peak components at binding energies of 284.8 and 287.9 eV corresponding to the presence of sp$^3$ and sp$^2$ hybridized carbons, respectively (Figure 4a). The sp$^3$ carbon peak originated from adventitious carbons, edge group carbons and turbostratic carbons present in the scaffold of $C_3N_5$ polymer while the relatively stronger sp$^2$ peak appeared due to N=C—N type aromatic carbons, which constitute the carbon nitride-like framework of $C_3N_5$.[25] The core level HR-XPS spectrum in N 1s region after deconvolution gave two peak components located at 398.7 and 400.2 eV. The peak at a binding energy of 398.7 eV was assigned to tertiary N—(C)$_3$ and secondary C=N—C nitrogens present in the aromatic ring structure while another peak at 400.2 eV was due to the presence of primary residual —NH$_2$ and bridging C—N=N—C type nitrogens (Figure 4b).[25,26] From the N 1s XPS spectrum, the at. % of N present in aromatic ring ($N_{ring}$) and bridging ($N_{bridging}$) were found to 60.47% and 39.53% respectively, and the at. % ratio obtained was 3:2, which strongly supports the proposed structure in which two heptazine units are interconnected with the azo ($-N=N-$) motif and is also consistent with the theoretical $C_3N_5$ azo-linked structure (Table 1). Furthermore, HR-XPS in Na 1s region gave a peak at 1071.9 eV due to the presence of Na$^+$ ions in the polymeric skeleton and residual NaCl (Figure S2b). The two peak components in Cl 2p XPS, at binding energy values of 198.7 and 200.2 eV ascribed to Cl 2p$_{3/2}$ and Cl 2p$_{1/2}$ further validated the presence of Cl$^-$ in the form of NaCl (Figure S2c). Two XPS peaks in the O 1s region located at 531.6 and 532.4 eV were associated with surface adsorbed adventitious oxygens and —OH groups (Figure S2d). The nature of C and N bonding in g-$C_3N_4$ and $C_3N_5$ was elucidated with electron energy loss spectroscopy (EELS) (Figure 4c,d and Figure S3). The normalized EELS spectra of g-$C_3N_4$ and $C_3N_5$ exhibited two major symmetric peaks due to contribution of C and N K-edge loss. The C K-edges signal of both g-$C_3N_4$ and $C_3N_5$ was composed of two peaks located at 284.6 and 293.2 eV corroborated to 1s-$\pi$* and 1s-$\sigma$* electronic transition of sp$^2$ hybridized carbons trigonally coordinated with nitrogens in s-heptazine nucleus (Figure 4c).[14a,b,27] The relative intensity of $\pi$* C K-edge signal and $\pi$*/$\sigma$* peak area ratio of $C_3N_5$ was higher than g-$C_3N_4$ suggesting
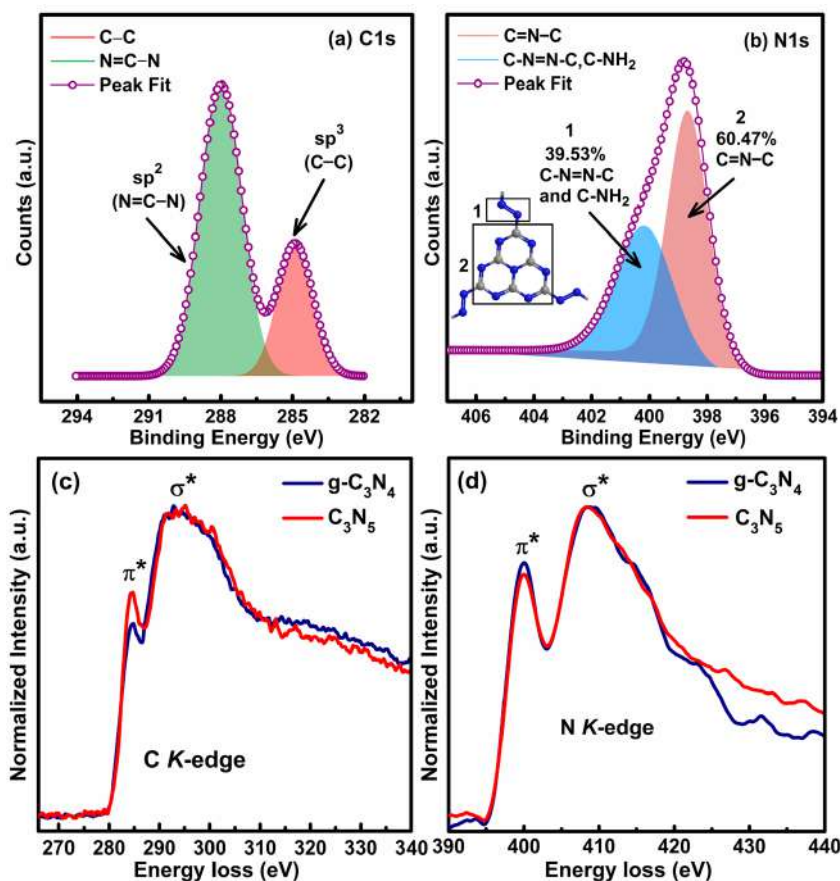
**Figure 4.** Core level HR-XPS spectra of $C_3N_5$ in (a) C 1s region, (b) N 1s region and normalized EELS spectra of g-$C_3N_4$ and $C_3N_5$ showing relative intensity of $\pi^*$ and $\sigma^*$ peaks for (c) C K-edge and (d) N K-edge loss.

**Table 1. (a) Elemental Analysis of $C_3N_5$ Showing C, H and N wt % and Empirical Formula and (b) XPS Elemental Analysis of $C_3N_5$ Showing at. % and Empirical Formula and Their Comparison with Theoretical $C_3N_5$ Composition**

| (a) elemental analysis | | | | | | |
|---|---|---|---|---|---|---|
| serial. no. | | N (wt %) | C (wt %) | H (wt %) | empirical formula | $N_{ring}:N_{bridging}$ (at. % ratio) |
| 1 | CHN analysis | 61.27 | 31.81 | 2.68 | $C_3N_{4.95}H_{1.01}$ | – |
| 2 | theoretical wt % value | 66.02 | 33.98 | – | $C_3N_5$ | 3:2 (60:40) |
| (b) XPS elemental analysis | | | | | | |
| serial. no. | | N (at. %) | C (at. %) | H (at. %) | empirical formula | $N_{ring}:N_{bridging}$ (at. % ratio) |
| 3 | XPS analysis | 63.24 | 36.76 | – | $C_3N_{5.16}$ | ∼3:2 (60.47:39.53) |
| 4 | theoretical at. % value | 62.50 | 37.50 | – | $C_3N_5$ | 3:2 (60:40) |

increased conjugation in $C_3N_5$ due to extended $\pi$ orbital overlap between bridging azo functionalities and heptazine motifs.[28] The formation of extended $\pi$ conjugated network in $C_3N_5$ was also supported by increased UV−vis absorption profile and shorter TRPL lifetime decay (Figures 7 and 8). The N K-edges energy loss peaks for g-$C_3N_4$ and $C_3N_5$ located at 399.8 and 408.5 eV, assigned to 1s-$\pi^*$ and 1s-$\sigma^*$ electronic transition of sp² hybridized nitrogens in heptazine ring and bridging N, further verify sp² hybridized nitrogen-rich carbon nitride framework (Figure 4d).[13] Absence of any new peak in N K-edge loss of $C_3N_5$ demonstrate bridging nitrogens in $C_3N_5$ have almost identical electronic environment to $N(C)_3$ nitrogens in g-$C_3N_4$.[29] The relative peak intensity of the N K-edge $\pi^*$ signal of $C_3N_5$ was slightly lower than that of g-$C_3N_4$, demonstrating enhanced contribution of azo motifs in 1s-$\sigma^*$ transition. The replacement of tertiary bridging nitrogens, $N(C)_3$ in g-$C_3N_4$ via azo nitrogens, C—N=N—C,

renders a lone pair on azo nitrogens, which contributes to $\sigma^*$ signal and relative intensity of $\pi^*$ signal suppressed. However, the total peak area of the N K-edge peak for $C_3N_5$ was increased, which demonstrated addition of extra nitrogens in the carbon nitride framework. The N:C atomic ratio of $C_3N_5$ was calculated to be 1.62, which was in close agreement with the theoretical value (1.66) and C:N value obtained from CHNS analysis (1.65). Slightly lower N content might be due to cleavage of azo bond resulting in loss of some nitrogens under high energy electron beam.

To probe the proposed composition and structure of the synthesized $C_3N_5$ material, CHNS elemental analysis was performed which gave 61.27 wt % N, 31.81 wt % C and 2.68 wt % H suggesting an empirical formula of $C_3N_{4.95}H_{1.01}$ which was in close proximity with the theoretical wt % for $C_3N_5$ composition (Table 1). Slight differences between predicted and observed C:N ratios might be due to the presence of
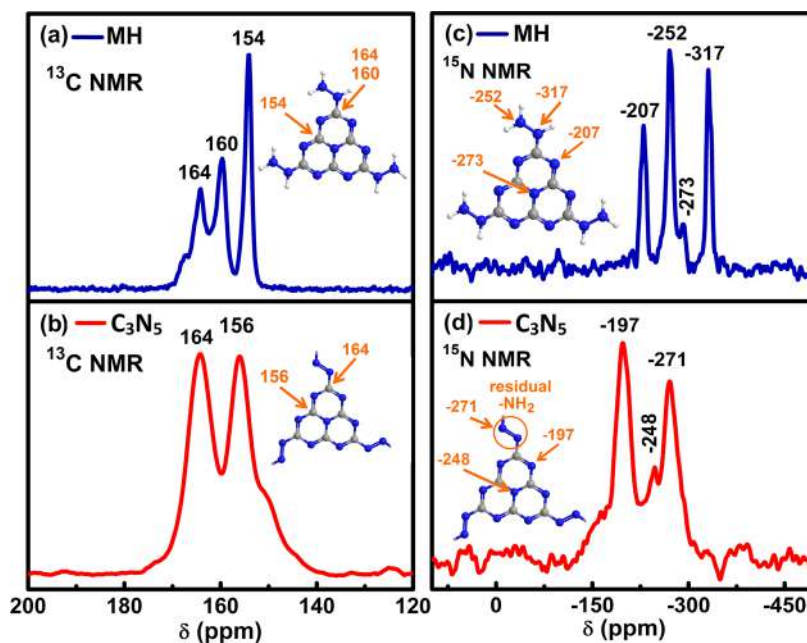
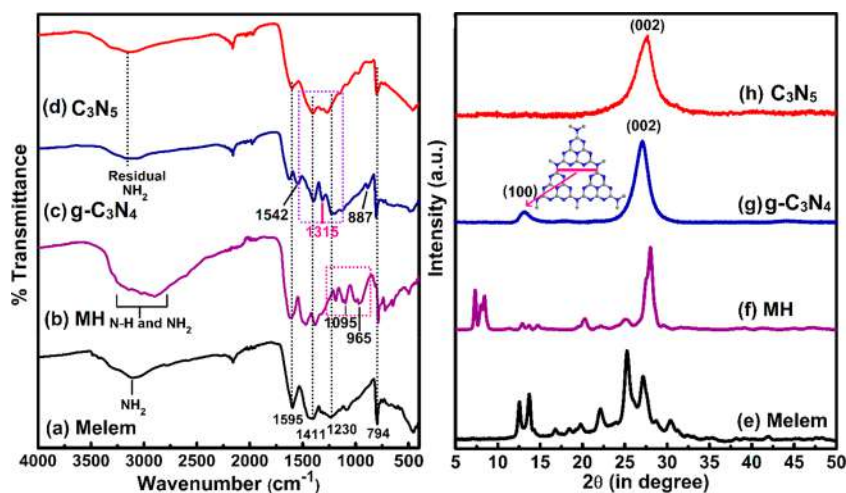**Figure 5.** CPMAS NMR spectra (a) $^{13}$C of MH, (b) $^{13}$C of C$_3$N$_5$, (c) $^{15}$N of MH and (d) $^{15}$N of C$_3$N$_5$.



**Figure 6.** FTIR spectra of (a) melem, (b) melem hydrazine, (c) g-C$_3$N$_4$, (d) C$_3$N$_5$, and XRD diffraction pattern of (e) melem, (f) melem hydrazine, (g) g-C$_3$N$_4$, (h) C$_3$N$_5$.

unbonded $-NH_2$ at the edge of sheets, formed by cleavage of hydrazino group $(-NH-NH_2)$ at elevated temperature and loss of some azo nitrogens.[9b,10b] As expected, sulfur was not present at measurable levels. Notably, the observed hydrogen might arise from $-NH_2$ and $-OH$ groups present at the edge of the polymeric framework.

To elucidate the chemical structure of MH and C$_3$N$_5$ materials, solid-state nuclear magnetic resonance (NMR) spectroscopy using the cross-polarization magic-angle spinning (CPMAS) technique was performed (Figure 5). CPMAS NMR enables the structural investigation of local- and medium-range structure in micro- and nanocrystalline compounds. The $^{13}$C CPMAS NMR spectra of melem hydrazine (MH) display three NMR signals at 164, 160 and 154 ppm (Figure 5a). The $^{13}$C NMR signals at 164 and 160 ppm originated from $N_2C-NHNH_2$ carbons while the resonance at 154 ppm was observed from $CN_3$ carbons of the heptazine nucleus. The observed signals were in good

agreement with the reported NMR spectra for MH and melem based structures.[18a,24,30] The CPMAS NMR spectrum of C$_3$N$_5$ exhibits two $^{13}$C NMR signals of approximately equal intensity at 164 and 156 ppm for $N_2C-N{=}N-$ and $CN_3$ carbons (Figure 5b).[24,30,31] The $N_2C-NHNH_2$ carbon signal of MH located at 160 ppm arising due to C−H functionalities disappeared in the $^{13}$C NMR of C$_3$N$_5$, which confirms removal of $-NHNH_2$ protons and formation of an azo linkage during polymerization step agreeing with $^{15}$N CPMAS NMR, *vide infra*. Although CPMAS is a non-quantitative approach, the appearance of equally intense (Cc:Ce/1:1.07) $^{13}$C peaks in the $^{13}$C NMR spectrum of C$_3$N$_5$ suggests that heptazine units are in the presence of a symmetric azo bridging motif (where Cc corresponds to central carbons in ring and Ce to external carbons bonded to azo N). A slight shift to higher frequency in $CN_3$ carbon peaks from 154 ppm in MH to 156 ppm in C$_3$N$_5$ suggests deshielding of carbons due to N 2p overlap of azo and aromatic $\pi$ system, which extends the $\pi$ conjugated network.[32]

The $^{15}N$ CPMAS NMR spectrum of MH exhibits four signals, $-207$, $-252$, $-273$ and $-317$ ppm (Figure 5c).[23a] The $^{15}N$ NMR signal at $-207$ ppm and another weak signal at $-273$ ppm were assigned to $(NC_2)$ and $(NC_3)$ nitrogens of the heptazine motif,[23a,31b,32,33] while the peaks at $-252$ and $-317$ ppm assigned to $NH_2$ and $NH$ terminal nitrogens of hydrazino moiety.[33,34] The transformation of MH to $C_3N_5$ proceeds with removal of $NH_3$ and formation of azo linkage which was evident from the disappearance of $NH_2$ and $NH$ peaks at $-252$ and $-317$ ppm in the $^{15}N$ NMR spectrum of $C_3N_5$ (Figure 5d). The two NMR peaks in the $^{15}N$ NMR spectra of $C_3N_5$ at $-197$ and $-248$ (weak) ppm were attributed to $NC_2$ and $NC_3$ nitrogens of heptazine skeleton while another peak at $-271$ ppm arose from $-N=N-$ (and residual NHs) type nitrogens. As the N atoms are in similar chemical environments, a semiquantitative CPMAS NMR analysis of the $^{15}N$ peak areas achieved by peak integration of $NC_2$ and $NC_3$ and $-N=N-$ resonances was found give a ratio of 1.00:0.18:0.54, which was in good agreement with the theoretical value (1.00:0.17:0.5) calculated for $C_3N_5$ polymeric structure containing heptazine units interconnected with azo linkage (Figure 1). Furthermore, $^1H$ NMR of MH gave an intense peak at 5.1 ppm due to NH and $NH_2$ hydrogens (Figure S4). This intense peak disappeared in the $^1H$ NMR spectra of $C_3N_5$ further confirming the removal of NH hydrogens and a very broad peak centered at 9 ppm appeared; this may be due to intercalated hydrogen, structural disorder, and residual terminal aldehyde and/or carboxylic acid hydrogens (essential for the CPMAS approach to function whereby $^1H$ magnetization is transferred to $^{13}C$ and $^{15}N$). All these NMR results validate the successful synthesis of a modified carbon nitride framework.

Fourier transform infrared (FTIR) spectroscopy was employed to determine the change in functional moiety in the material (Figure 6a–d). The FTIR spectrum of melem shows characteristic broad peaks at 3109 cm$^{-1}$ due to the combined symmetric and antisymmetric stretch vibrations of $-NH_2$ and $-OH$ ($\nu_{N-H}$ and $\nu_{O-H}$) groups. The IR bands at 1595, 1411, 1230 and 1078 cm$^{-1}$ are ascribed to the C–N stretch ($\nu_{C-N}$) of heptazine ($C_6N_7$) aromatic nucleus (Figure 6a).[18a,31b,34a,35] The N–H stretch band ranging from 3153 to 2895 cm$^{-1}$ for MH was found to become broader due to combinational symmetric and asymmetric N–H stretches of $-NH-NH_2$ group in MH, which confirms the successful transformation of $-NH_2$ moiety in melem to $-NH-NH_2$ in melem hydrazine (Figure 6b). The broadening of the NH peak was attributed to strong intermolecular hydrogen bonding in MH molecules.[35,36] However, all stretching and bending peaks due to heptazine aromatic ring skeleton remain preserved, which indicates that the heptazine motif remains unchanged during the hydrazine treatment. Additionally, some new peaks emerged at 1095 and 965 cm$^{-1}$ implicating the N–N stretch and $-NH_2$ rocking vibration, respectively.[18a,36,37] Graphitic carbon nitride shows characteristic peaks at 3145 cm$^{-1}$ due to residual $-NH_2$ and $-OH$ stretch and 1639–1145 cm$^{-1}$ due to triazine ring stretch and 798 cm$^{-1}$ for triazine ring bending vibration was in good agreement with the reported literature (Figure 6c).[37,38] After conversion of MH to $C_3N_5$ by thermal annealing, the intensity of $-NH-NH_2$ peak of MH was diminished which implicated the transformation of $-NH-NH_2$ group into azo ($-N=N-$) linkage through the removal of $NH_3$ (Figure 6d). It is important to note that vibration of symmetrical $-N=N-$ azo linkage is forbidden due to which

no new sharp peak due to azo functionalities was observed. The possibility of $-NH-NH-$ bond can be neglected due to the absence of any strong N–H band; however, very weak broad peaks arise due to some residual $-NH_2$ present at the edge of the polymeric framework. This fact was well supported by CHNS analysis, which showed the presence of only one H for each stoichiometric $C_3N_5$ unit (Table 1). Further, other peaks of MH at 1095 and 965 cm$^{-1}$ due to N–N stretch and $-NH_2$ rocking vibration disappear in $C_3N_5$, which confirmed the transformation of hydrazine group into azo moiety. Peaks corresponding to the $C_3N_4$ framework at 1542, 1315 and 887 cm$^{-1}$ were absent in $C_3N_5$, which suggests an entirely different network of $C_3N_5$ in comparison to g-$C_3N_4$.

The changes in phase structure and crystalline nature of melem, MH, g-$C_3N_4$ and $C_3N_5$ were investigated through the measurement of X-ray diffraction (XRD) (Figure 6). The XRD pattern of melem demonstrated a series of peaks located at 12.5°, 13.6°, 16.7°, 18.4°, 19.7°, 22.0°, 25.2°, 27.2° and 30.4°, in close agreement with previous reports (Figure 6e).[38,39] The XRD results indicate the absence of any melamine impurity in the melem sample.[18b,39a] Because of the transformation of melem into melem hydrazine, the XRD pattern of MH changed, with new peaks being observed at $2\theta$ values of 7.3°, 7.9°, 8.4°, 12.9°, 13.7°, 14.8°, 25.1° and 28.0° (Figure 6f). Bulk g-$C_3N_4$ shows two distinct XRD peaks at $2\theta$ values of 27.1° and 13.0° indexed to the 002 and 100 planes of carbon nitride materials (Figure 6g). The 002 peak with a 0.32 nm interplanar $d$ spacing was correlated to interplanar stacking of sheets while the 100 peaks with a 0.68 nm spacing was specific to in-plane structural packing of heptazine units (Figure 6g).[18b,39b,40] The XRD pattern of $C_3N_5$ exhibits one broad 002 peak at 27.6° corresponded to 0.33 nm interplanar sheet distance. The slight increase in $2\theta$ value and $d$ spacing can be explained due to repulsion between electron-rich $\pi$ conjugated $C_3N_5$ sheets as in graphite (0.34 nm) (Figure 6h). Further, the absence of a 100 peak, a specific feature of in-plane packing, suggests distortion in the carbon nitride framework and broadening of the nanochannel distance between heptazine units due to azo ($-N=N-$) bridging linkage, consistent with $^{13}C$ and $^{15}N$ NMR resonance broadening above, suggesting local/medium-range disorder. Also, bridging of two heptazine units with two nitrogens through in-plane lattice packing is less efficient in $C_3N_5$ which was responsible for the absence of any expected peak at lower $2\theta$ values. These XRD results clearly support the distinct structure of $C_3N_5$ possessing azo linkage.

Raman spectra of melem acquired using 632 nm laser excitation show characterstic fingerprint peaks of melem at 435 and 697 cm$^{-1}$ due to heptazine ring ($C_6N_7$) breathing modes and a broad hump at 1452 cm$^{-1}$ due to $-NH_2$ bending mode (Figure S5a).[18a,40a] Raman spectra of MH demonstrate many signature peaks correlated to the core at 472, 744 and 1529 cm$^{-1}$, which were shifted in comparison to melem due to functionalization while other peaks due to various vibrations of the heptazine nucleus and hydrazine group were observed at 127, 342, 537, 985, 1159, 1314 and 3071 cm$^{-1}$, in good agreement with the reported literature (Figure S5b).[18a,23a,40b,41] The Raman spectra of g-$C_3N_4$ display many prominent peaks due to the heptazine framework at 471, 697 and 706 cm$^{-1}$ (heptazine ring breathing modes) and two additional peaks at 1233 and 1567 cm$^{-1}$ corresponding to the $-NH_2$ bending mode and graphitic G band (Figure S5c).[23a,42] Further, the presence of a broad hump extended from 1100 to 1600 cm$^{-1}$ suggests multilayer stacking of g-$C_3N_4$ sheets.[41,43]
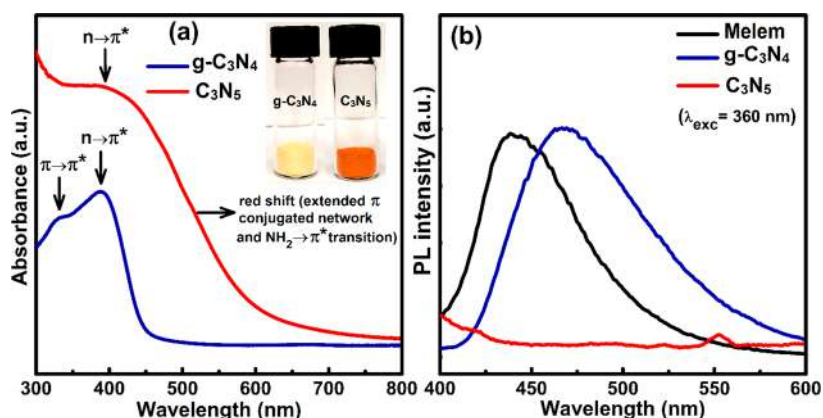
**Figure 7.** (a) DR-UV−vis spectra of g-C$_3$N$_4$ (blue) and C$_3$N$_5$ (red), with inset showing photographs of g-C$_3$N$_4$ and C$_3$N$_5$ samples and (b) Steady-state PL spectra of melem (black), g-C$_3$N$_4$ (blue) and C$_3$N$_5$ (red) obtained using an excitation wavelength of 360 nm.
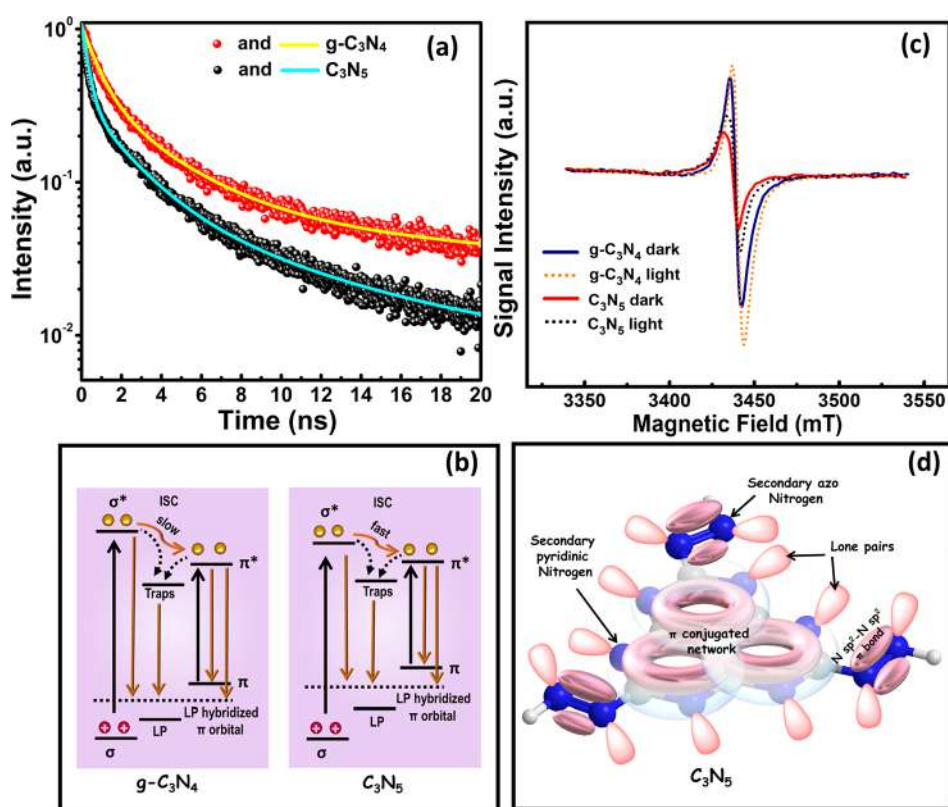


**Figure 8.** (a) PL lifetime decay curves of g-C$_3$N$_4$ (red; triexponential fit, yellow line) and C$_3$N$_5$ (black, triexponential fit, cyan), (b) Schematics of various energy level bands and possible route of charge carrier recombination (c) X-band EPR spectra of g-C$_3$N$_4$ in the dark (blue), after light irradiation (orange dots) and C$_3$N$_5$ in the dark (red) and after light irradiation (black dots) at room temperature, (d) Plausible molecular orbital overlap representation of C$_3$N$_5$.

In the Raman spectra of C$_3$N$_5$, only trace peaks of melem hydrazine motif are observed which indicates the complete transformation of MH to C$_3$N$_5$. Two small peaks were observed at 1085 and 1161 cm$^{-1}$ due to the mixed vibration of heptazine motif and azo stretch (Figure S5d). A sharp peak at 1609 cm$^{-1}$ originated due to the C≡N stretching mode.

Figure 7a displays the diffuse reflectance UV−vis (DR-UV−vis) spectra of g-C$_3$N$_4$ and C$_3$N$_5$. The DR-UV−vis spectrum of g-C$_3$N$_4$ shows a characteristic absorption peak between 200 and 400 nm with a band tail extended up to 450 nm due to charge transfer from the populated valence band of the nitrogen atom (2p orbitals) to the conduction band of the carbon atom (2p orbitals) of carbon nitride. The less intense absorption band at 330 nm is due to $\pi \rightarrow \pi^*$ transition in the conjugated network while another intense peak at ca. 387 nm appeared due to $n \rightarrow \pi^*$ transition from nitrogen nonbonding orbital to the aromatic nonbonding orbital.[12b,42−44] The DR-UV−vis spectrum of C$_3$N$_5$ demonstrates a drastic change in the UV−vis absorption profile in comparison to g-C$_3$N$_4$ due to a more extended $\pi$ conjugated network (Figure 7a).[12b,45] A broad absorption peak around 393 nm in UV−vis spectrum of C$_3$N$_5$ was attributed to $n \rightarrow \pi^*$ transition from nitrogen nonbonding orbital to the $\pi$ conjugated nonbonding orbital. The absorption spectrum of C$_3$N$_5$ was red-shifted showing

band tailing up to 670 nm, due to an extended $\pi$ conjugated network arising from the overlap between N 2p orbitals of bridging azo moieties and N 2p in heptazine $\pi$ conjugated system. Further residual $-NH_2$ also contributes to the delocalized aromatic $\pi$ conjugated system. Because of this, the position of the valence band gets upshifted and $\pi \rightarrow \pi^*$ transition occurs at relatively low energy which facilitates the absorption of a large fraction of the visible spectrum and results in the sample displaying an orange color. Further, the optical bandgaps of g-$C_3N_4$ and $C_3N_5$ were determined using a Tauc plot by plotting a graph between $(\alpha h\nu)^{1/2}$ vs $h\nu$ and extrapolation of the linear tangent to abscissa; where $\alpha$ is absorption coefficient, $h$ is plank constant and $\nu$ is light frequency (Figure S6a). From the Tauc plot, the value of bandgap for g-$C_3N_4$ was estimated to be 2.65 eV corresponding to a band-edge at a wavelength of 467 nm, in good agreement with the bandgap values reported in the literature.[46] The bandgap value of $C_3N_5$ was calculated to be 1.76 eV corresponding to a band-edge at a wavelength of 707 nm.

Photoluminescence (PL) spectra were collected by exciting samples using 360 nm photons to probe radiative recombination (Figure 7b). The PL spectrum of melem consists of an intense emission peak centered at 441 nm, which is indicative of radiative recombination of carriers within the melem unit.[39a,44] It is important to note here that melem exhibits excitation wavelength-dependent PL emission. On the other hand, g-$C_3N_4$ showed a sharp emission peak at 468 nm, which did not shift upon changing the excitation wavelength. This peak is attributed to fast interlayer carrier recombination in multilayered sheets of bulk g-$C_3N_4$.[45,47] Surprisingly, $C_3N_5$ does not exhibit any distinguishing PL peak, which might be indicative of efficient charge separation between the bulk and the surface. Such charge transfer excitonic states involving the bulk and the surface have also been observed in other conjugated organic semiconductors that possess an extended $\pi$-conjugated network that prevents radiative recombination by delocalizing the Frenkel exciton. However, because of conductive conjugated surface, nonradiative charge recombination can take place over new localized states in the sheets scaffold.[48]

In order to investigate the lifetime of excited charged species, and charge separation processes, we collected time-resolved photoluminesece (TRPL) spectra of g-$C_3N_4$ and $C_3N_5$ using a single photon picosecond pulsed laser at a wavelength of 405 nm. Figure 8a displays the PL lifetime decay curves of g-$C_3N_4$ and $C_3N_5$. The PL decay curve was fitted triexponentially using the following equation:

$$I(t) = A_1 e^{-t/\tau 1} + A_2 e^{-t/\tau 2} + A_3 e^{-t/\tau 3} \qquad (1)$$

where, $A_1$, $A_2$ and $A_3$ represent the normalized amplitudes of each decay component and $\tau_1$, $\tau_2$ and $\tau_3$ are values of the lifetime components, respectively. The existence of three radiative lifetimes in the fitted PL lifetime spectra of g-$C_3N_4$ and $C_3N_5$ was in good agreement with previously reported carbon nitride based materials.[49] The obtained values of lifetimes and their fractional components are given in Table 2.

The three components in the PL lifetime decay curve of g-$C_3N_4$ can be assigned to various energy states in g-$C_3N_4$ formed by the overlap of C and N $sp^2$ and $sp^3$ hybridized orbitals and the presence of lone pairs of electrons, which allow for various radiative transitions (Figure 8b). g-$C_3N_4$ is composed of tri-$s$-triazine ($C_6N_7$) units interconnected with

**Table 2. PL Lifetime of Phogenerated Charge Carrier and Their Relative Contribution in g-$C_3N_4$ and $C_3N_5$**

| sample | $\tau_1$ (ns) $[A_1]$ | $\tau_2$ (ns) $[A_2]$ | $\tau_3$ (ns) $[A_3]$ | average lifetime ($\tau_{avg}$, ns) |
|---|---|---|---|---|
| g-$C_3N_4$ | 3.31 [0.34] | 0.75 [0.63] | 25.02 [0.05] | 12.43 |
| $C_3N_5$ | 8.10 [0.07] | 2.11 [0.26] | 0.28 [0.73] | 4.40 |

tertiary nitrogen atoms where C—N $sp^3$ hybridized state constitute high energy $\sigma$ and $\sigma^*$ molecular orbitals while C—N $sp^2$ hybridization gives rise to a conjugated network resulting in low energy $\pi$ bonding and $\pi^*$ antibonding orbital, which constitutes the valence and conduction bands, respectively.[50] The presence of unbonded lone pairs of electrons on pyridinic N atoms creates energy levels just below the $\pi$ bonding orbital and their overlap with the $\pi$ conjugated system can further decrease the energy of the $\pi$ molecular orbital resulting in the reduction of the bandgap.[51] The first two shorter lifetime components of 3.31 and 0.75 ns with 34% and 63% contribution in g-$C_3N_4$ correspond to charge carrier recombination from $\sigma^*$ and $\pi^*$ antibonding to $\pi$ MO.[52] The third longer lifetime component of 25.02 ns with a relative low contribution originated due to intersystem crossing (ISC) of electron from $\sigma^*$ to $\pi^*$ orbital followed by radiative relaxation to conjugated $\pi$ orbital and trap-assisted radiative recombination.[53] The first two lifetimes of $C_3N_5$ at 8.10 and 2.11 ns with 7% and 26% contributions in the PL decay curve were significantly longer lived in comparison to g-$C_3N_4$, suggesting that the introduction of azo moiety extends $\pi$ conjugated network which facilitates better charge carrier mobility on $C_3N_5$ sheets (delocalized the exciton, as mentioned previously) and prevents faster charge carrier recombination.[54] Further, because of extended conjugation, the difference between $\sigma^*$ and $\pi^*$ band gets decreased, which is also evident in Mott—Schottky measurement (Figure S6b).[51a] The low energy difference between $\sigma^*$ and $\pi^*$ accelerates the transfer of electrons from $\sigma^*$ and $\pi^*$ orbital via intersystem crossing followed by radiative relaxation, which was evident from higher percentage contribution of the third lifetime component (73%).

The average lifetime ($\tau_{avg}$), which is regarded as a coherent measure to evaluate the rate of spontaneous emission, was calculated from the three lifetime components using the following expression:

$$\tau_{avg} = (A_1\tau_1^2 + A_2\tau_2^2 + A_3\tau_3^2)/(A_1\tau_1 + A_2\tau_2 + A_3\tau_3)$$

$$(2)$$

From eq 2, the average lifetimes of g-$C_3N_4$ and $C_3N_5$ were calculated to be 12.43 and 4.40 ns, respectively. The decreased lifetime of the $C_3N_5$ in comparison to g-$C_3N_4$ coupled with the very weak photoluminescence of $C_3N_5$ (as shown in Figure 7b) is indicative of fast quenching of the $C_3N_5$ luminescence. The fast quenching might originate from improved charge separation in $C_3N_5$ due to a larger conjugated $\pi$ network but might also be due to stronger nonradiative transitions. Fast exciton dissociation with concomitant high carrier mobility can result in photogenerated electrons finding trap sites (and moving to them) and recombining by nonradiative processes.[48a] The aforementioned processes are likely in $C_3N_5$ since the presence of azo bonds extends the $\pi$ network because of overlap of N 2p orbital on azo nitrogens with the $\pi$ network of heptazine motif due to which electrons can move within $C_3N_5$ scaffold freely. The lower PL lifetime of $C_3N_5$ in comparison to
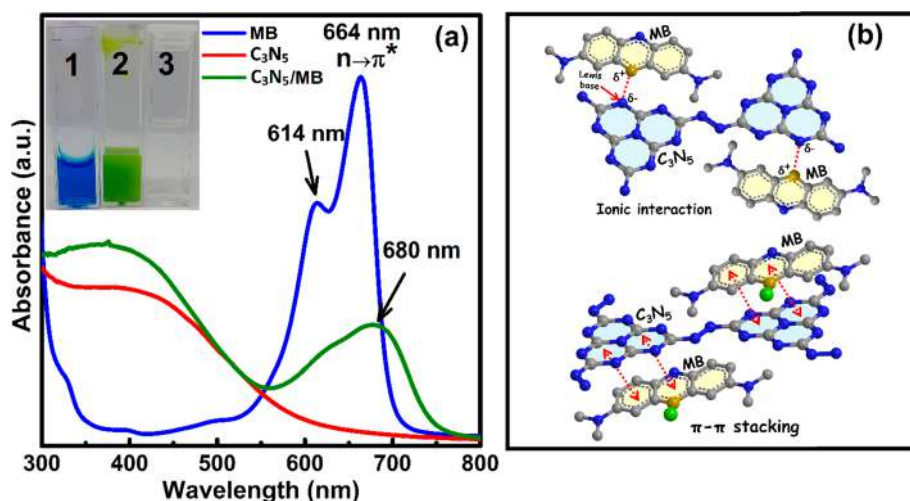
**Figure 9.** (a) UV−vis absorption spectra of MB (blue), $C_3N_5$ (red) and $C_3N_5$/MB solution just after 1 min of absorption (green). Inset shows photographs of (1) MB before absorption, (2) after absorption and (3) solution after centrifugation. (b) Possible ionic and $\pi−\pi$ stacking interaction between methylene blue and $C_3N_5$.

g-$C_3N_4$ was consistent with steady-state PL where $C_3N_5$ shows prodigious quenching in its PL spectrum.

Electron paramagnetic resonance (EPR) spectra of g-$C_3N_4$ and $C_3N_5$ to elucidate electronic nature and band excited paramagnetic species were collected under dark and UV irradiation at room temperature (Figure 8c). The EPR spectra of g-$C_3N_4$ under dark conditions exhibits an intense Lorentzian EPR resonance signal located at a g-factor of 2.003. The observed EPR signal originated due to the presence of unpaired electrons in the sp$^2$ hybridized aromatic $\pi$-system which was in good agreement with previous reports.[36,55] The EPR signal intensity of g-$C_3N_4$ increased after UV irradiation, attributed to populated unpaired electrons in the conduction band due to $\pi−\pi$* and N nonbonding to $\pi$* (n−$\pi$*) transition followed by slow relaxation via ISC. The observed EPR signal of $C_3N_5$ was also observed at 2.003 g-value, which implies basic graphitic heptazine skeleton remains intact in $C_3N_5$ framework.[56] Further, after irradiation with UV light, the EPR signal intensity of $C_3N_5$ was also enhanced due to increased numbers of unpaired electrons in the conduction band. However, the overall EPR signal intensity of $C_3N_5$ in both the dark and under UV illumination was significantly weaker in comparison to g-$C_3N_4$, which was attributed to a lesser number of unpaired electrons in $C_3N_5$, which in turn can be taken as evidence of the presence of extra N atoms outside the heptazine nucleus in comparison to conventional N-rich carbon nitride materials where N atoms substitute C atoms in the heptazine motif. It is well documented in the literature that substitution of sp$^2$ hybridized +4 state C atom in heptazine motif with sp$^2$ hybridized +3 state N atom will liberate extra electrons in the aromatic system, which will distort electronic symmetry[16,47,57] and also increase EPR signal intensity. However, in the case of $C_3N_5$, the additional N atom makes an azo bond with an N atom outside the ring via $\pi$ overlap and the extra electrons remain in the form of lone pairs (Figure 8d).

Fluorescence lifetime imaging microscopy (FLIM) of samples at different spots was used to probe the homogeneity of samples and to determine the nature of the fluorescence (Figure S7). The PL spectra of g-$C_3N_4$ samples obtained from different spots exhibited identical emission profiles with a sharp intense peak at 480 nm, which was in good agreement with the steady-state PL spectrum (Figure 7b). The slight red shift in the emission peak (Figure S7a) is attributed to the difference in the mechanism of excitation (750 nm two-photon excitation source for FLIM, 360 nm single photon excitation in ssPL Figure 7b). Furthermore, the emission spectrum of $C_3N_5$ displays two relatively weak peaks centered around 410 and 490 nm which likely originated from some relatively smaller $C_3N_5$ polymeric fragments and heptazine networks (Figure S7c). The smaller fragments are constituted with a lesser number of MH units and therefore exhibit PL properties closer to melem. FLIM images of g-$C_3N_4$ were brighter than $C_3N_5$ which further supports our inference that the charge separation process was dominant in $C_3N_5$ samples (Figure S7b,d). The $C_3N_5$/MB samples obtained after methylene blue (MB) dye adsorption displayed relatively strong PL and brighter FLIM images due to the presence of MB in the composite (Figure S7e,f). The absence of PL quenching in the $C_3N_5$/MB composite further suggests the absence of photoinduced charge transfer between the methylene blue and $C_3N_5$.

The synthesized $C_3N_5$ material was explored for dye adsorption studies using methylene blue (MB) as a model dye. Methylene blue is a staining dye widely used in the paper, textile and leather industries which also constitutes a good example of a colored water contaminant, which due to its excellent visible light absorption, reduces light penetration in aqueous ambients and adversely affects aquatic flora and fauna. All dye adsorption studies were carried out at room temperature and under dark conditions. UV−vis spectra of samples were collected for determining the concentration of MB solutions during dye adsorption experiments (for experimental details, see Supporting Information). MB has a sharp peak at 664 nm due to $\pi−\pi$* transition and a shoulder around 614 nm which represents MB present in dimeric and polymeric $\pi$ stacked forms in water (Figure 9a). After the addition of $C_3N_5$ sample into methylene blue solution, the color of the solution instantaneously turned green. The green solution after centrifugation turned completely colorless, which demonstrated the prompt adsorption of MB dye over the surface of $C_3N_5$ and subsequent settling of the MB adsorbed $C_3N_5$ during centrifugation. The obtained solid after centrifugation (denoted as $C_3N_5$/MB) exhibits a sharp
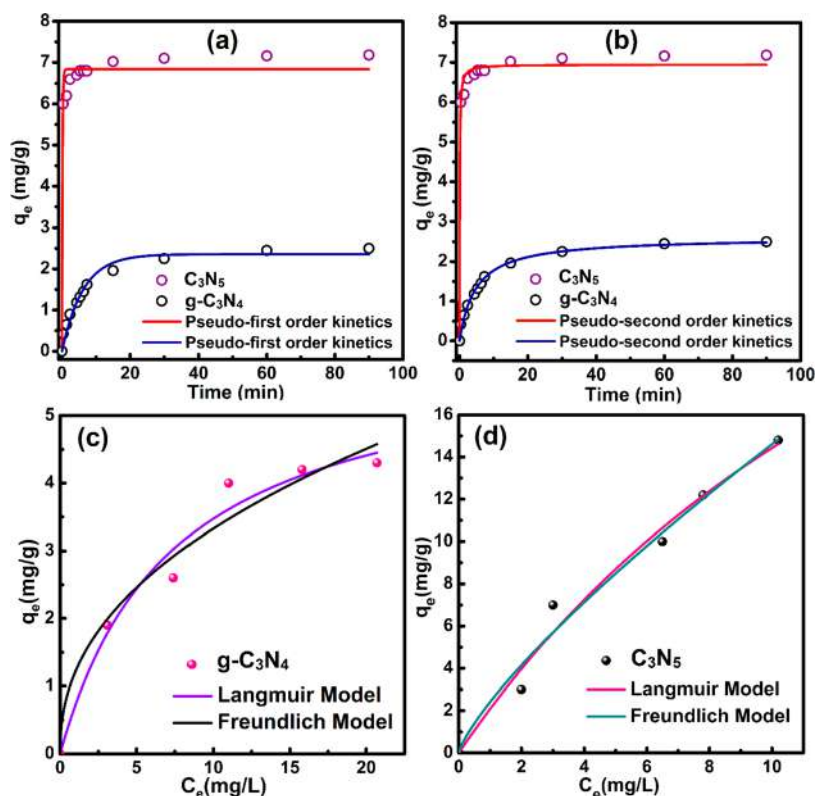
**Figure 10.** Kinetics of MB dye adsorption on g-C$_3$N$_4$ and C$_3$N$_5$ displaying (a) pseudo-first-order fitted curve, (b) pseudo-second-order fitted curve and MB adsorption isotherms fitted by Langmuir and Freundlich model of (c) g-C$_3$N$_4$ and (d) C$_3$N$_5$, respectively. $q_e$ is the amount of dyes adsorbed at equilibrium while $C_e$ is the equilibrium concentration of MB.

absorption peak intermediate between C$_3$N$_5$ and MB with a broad peak centered at 680 nm. The redshifting in the peak of MB from 664 to 680 nm is attributed to the transformation of MB into monomeric form and some degree of ground state charge transfer from C$_3$N$_5$ to MB during adsorption on the surface of C$_3$N$_5$. The dye adsorption performance of C$_3$N$_5$ was much higher than g-C$_3$N$_4$. MB is a well-known cationic dye possessing positive charge centered on the S atom in aqueous solutions.[58] On the other hand, the surface of C$_3$N$_5$ material has electron-rich character due to the presence of secondary N (NC$_2$) in heptazine moieties, terminal −NH$_2$ and π extended network. Therefore, electrostatic interactions between the positively charged MB molecule and negatively charged C$_3$N$_5$ are likely responsible for the instantaneous adsorption.[54,59] To confirm negative charge on the surface of C$_3$N$_5$, ζ-potential measurement was performed which depicts average surface charge of −36.2 mV and proves the electron-rich surface of C$_3$N$_5$ (Figure S8). Further, MB can also adsorb on the surface of C$_3$N$_5$ via π−π stacking between aromatic conjugated network of MB and π framework of C$_3$N$_5$ (Figure 9b).[60] To investigate the role of surface specific properties in the enhanced adsorption profile, Brunauer−Emmett−Teller (BET) surface area ($S_{BET}$), pore volume ($V_p$) and pore diameter ($r_p$) of g-C$_3$N$_4$ and C$_3$N$_5$ were measured by N$_2$ adsorption and desorption. The obtained BET surface area, pore volume and pore diameter for g-C$_3$N$_4$ were found to be 11.47 m$^2$ g$^{-1}$, 0.095 cm$^3$ g$^{-1}$ and 19.13 nm while these values for C$_3$N$_5$ were found to be 1.78 m$^2$ g$^{-1}$, 0.002 cm$^3$ g$^{-1}$ and 16.98 nm, respectively. The obtained surface values indicate a decrease in the surface area of C$_3$N$_5$ in comparison to g-C$_3$N$_4$. The relatively low surface area of C$_3$N$_5$ might be due to the

less gas evolution (three NH$_3$ per heptazine unit) from melem hydrazine precursor during thermal annealing step while the formation of g-C$_3$N$_4$ from melamine precursor releases six NH$_3$ molecule per heptazine unit. Further, hydrogen bonded melem hydrazine precursor might promote in-plane cross-linking of heptazine units leading to a stacked sheets type structure which reduces the effective accessible surface area. Contrarily, in g-C$_3$N$_4$ ring formation and polymerization step can produce cross-linking between sheets giving a porous structure with high surface area. The obtained results suggest that an electronic interaction between C$_3$N$_5$ and MB is responsible for the superior adsorption performance of C$_3$N$_5$ rather than an increased surface area.

To investigate whether the nature of adsorption was chemisorption or physisorption, and to explore the possibility of any chemical bonding, the C$_3$N$_5$/MB composite was analyzed using NMR spectroscopy. The $^{13}$C NMR spectrum of C$_3$N$_5$/MB composite did not show any change in peak position and intensity of C$_3$N$_5$, which demonstrated the adsorption of MB on C$_3$N$_5$ to be purely physisorptive in nature (Figure S9d). FTIR, Raman and PL spectra of C$_3$N$_5$/MB composite displayed various cumulative peaks and signals due to the presence of MB in the C$_3$N$_5$/MB composite. However, no evident signals for any chemical interaction can be identified, which further supports a purely physical interaction (physisorption) between C$_3$N$_5$ and MB (Figure S9a−c). Additionally, XPS spectra of C$_3$N$_5$/MB composite were identical to pristine C$_3$N$_5$ samples which revealed that C$_3$N$_5$ signals dominated over MB, and no change in BE value was observed which ruled out the possibility of any chemical bond formation between C$_3$N$_5$ and MB (Figure S10).

**Table 3. Pseudo-First- and Second-Order Kinetic Models of MB Adsorption on g-$C_3N_4$ and $C_3N_5$ and Langmuir and Freundlich Adsorption Models Showing Isotherm Constants**

| serial no. | sample name | pseudo-first-order | | | pseudo-second-order | | |
|---|---|---|---|---|---|---|---|
| | | $k$ (s$^{-1}$) | $q_e$ (mg g$^{-1}$) | $R^2$ | $k$ (s$^{-1}$ mg$^{-1}$ L) | $q_e$(mg g$^{-1}$) | $R^2$ |
| 1 | g-$C_3N_4$ | 0.16 | 2.35 | 0.96 | 0.08 | 2.6 | 0.99 |
| 2 | $C_3N_5$ | 6.35 | 6.83 | 0.98 | 2.24 | 6.95 | 0.99 |
| serial no. | sample name | Langmuir | | | Freundlich | | |
| | | $Q$ (mg g$^{-1}$) | $b$ (L mg$^{-1}$) | $R^2$ | $K$ (mg$^{1-n}$ L$^n$ g$^{-1}$) | $n$ | $R^2$ |
| 1. | g-$C_3N_4$ | 6.03 | 0.13 | 0.97 | 1.21 | 0.43 | 0.96 |
| 2. | $C_3N_5$ | 42.32 | 0.05 | 0.98 | 2.40 | 0.78 | 0.97 |
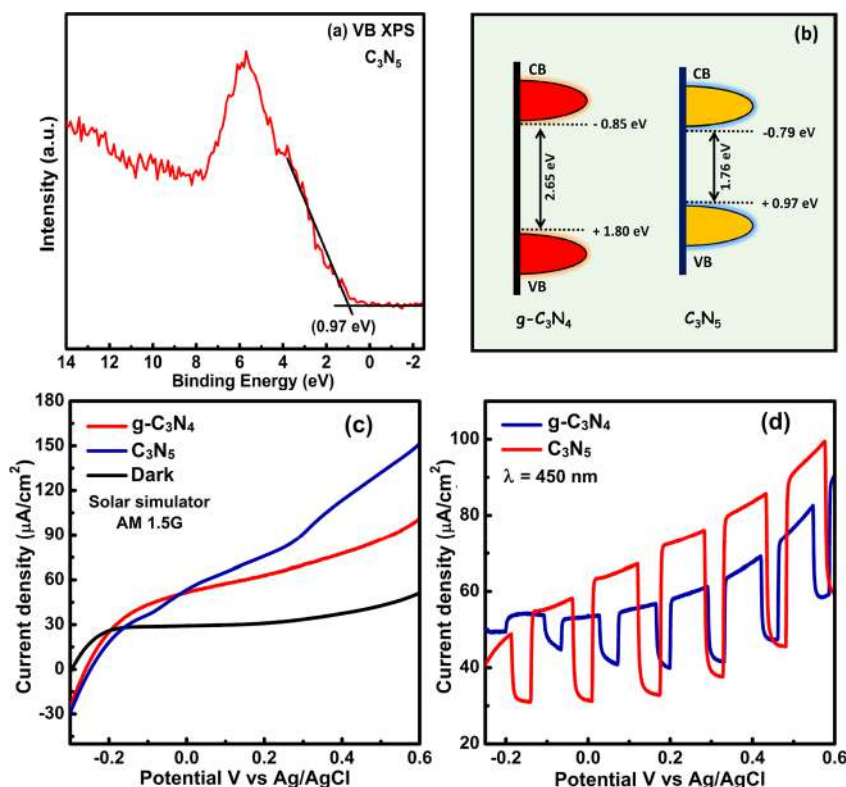


**Figure 11.** (a) XPS valence band spectra of $C_3N_5$ for determining energy levels. (b) Density of state revealing band structure of g-$C_3N_4$ and $C_3N_5$. (c) Linear sweep voltammogram showing current−potential characteristics of g-$C_3N_4$ (blue) and $C_3N_5$ (red) measured in 0.1 M $Na_2SO_4$ solution AM1.5G light irradiation (100 mW cm$^{-2}$) and under dark conditions. (d) Light on−off showing photocurrent response vs applied voltage by using 450 nm wavelength light (54.15 mW cm$^{-2}$) for g-$C_3N_4$ (blue) and $C_3N_5$ (red).

To quantify the excellent dye adsorption capacity of $C_3N_5$, various parameters such as the adsorption capacity, adsorption constants, linear regression correlation coefficient, and adsorption isotherm were measured and compared with pristine g-$C_3N_4$ (Figure 10 and Table 3). The adsorption capacity (amount of dye adsorbed) of g-$C_3N_4$ and $C_3N_5$ materials was calculated using eq 3:

$$q = \frac{(C - C_e)V}{m} \tag{3}$$

Where $q$ is the adsorption capacity, $V$ is the volume of MB solution, $m$ is the mass of the added adsorbent, and $C$ and $C_e$ are the initial and equilibrium concentrations of MB, respectively. The kinetics of methylene blue adsorption on the surface of g-$C_3N_4$ and $C_3N_5$ were investigated using first- and second-order adsorption kinetics using eqs 4 and 5:

$$q_t = q_e(1 - e^{-kt}) \tag{4}$$

$$q_t = \frac{kq_e^2 t}{1 + kq_e t} \tag{5}$$

Where $q_e$ is adsorbed amount of dye after reaching equilibrium and $q_t$ is the adsorbed amount at time $t$, and $k$ is the pseudo-first-order or pseudo-second-order adsorption rate constant.

The results obtained using pseudo-first-order and pseudo-second-order kinetics are displayed in Table 3 and Figure 10a,b. The kinetic studies clearly demonstrate that the prepared $C_3N_5$ samples can reach approximately 95% adsorption−desorption equilibrium instantaneously (1 min), and complete adsorption−desorption equilibrium within 10 min, which is an extraordinary performance compared to previously reported carbon nitride and carbon based materials which usually take 45 min to achieve equilibrium.[61] In addition, the kinetics study indicated that the adsorption of methylene blue on the $C_3N_5$ and g-$C_3N_4$ materials follows pseudo-second-order adsorption kinetics, which agreed well

with previous reports.[61a] For isotherm studies, standard solutions of 5, 10, 15, 20, 25 and 30 ppm MB in water were prepared; 50 mL of these standard solutions was placed in a beaker and 50 mg of the adsorbents was added to them. The solutions were kept under strong stirring for 30 min under dark conditions to reach equilibrium, and then the concentration of methylene blue was calculated using UV−vis spectroscopy (see Supporting Information for details). The adsorption isotherms of methylene blue were investigated in terms of the Langmuir[61b,62] and Freundlich models[61b,63] (eqs 6 and 7, respectively), and the results for g-$C_3N_4$ and $C_3N_5$ are displayed in Figure 10c,d, respectively; the relevant constants are reported in Table 3. It can be seen from Figure 10 and Table 3 that the value of $R^2$ extracted by employing the Langmuir isotherm model was higher than the $R^2$ value obtained from the Freundlich isotherm model, indicating that the Langmuir model representing complete monolayer coverage on homogeneous sites was successful in predicting the adsorption of methylene blue on both g-$C_3N_4$ and $C_3N_5$.[64]

$$q_e = \frac{QbC_e}{(1 + bC_e)} \qquad (6)$$

$$q_e = KC_e{}^n \qquad (7)$$

Where $q_e$ is adsorbed amount of dye after reaching equilibrium (mg g$^{-1}$), $R$ is correlation coefficient, $Q$ is the monolayer adsorption capacity (mg g$^{-1}$), $b$ is the adsorption coefficient (L mg$^{-1}$), $C_e$ is the equilibrium concentration and $K$ is the Freundlich constant.

To check whether $C_3N_5$ material displays any visible light induced dye degradation activity, 50 mL of 50 ppm MB containing solution was charged with 50 mg of $C_3N_5$ catalyst and stirred in the dark for 30 min to reach adsorption−desorption equilibrium. Subsequently, the obtained suspension was irradiated under simulated sunlight (AM1.5G, 100 mW cm$^{-2}$). After every 10 min, 1 mL of sample was withdrawn and centrifuged to remove solid $C_3N_5$ and the supernatant liquid was analyzed with UV−vis spectroscopy. The UV−vis analysis indicated that the concentration of MB solution does not change even after 8 h of irradiation. These results suggest that $C_3N_5$ is not active for dye degradation, which might be because of unfavorable band alignment. To understand the band structure of $C_3N_5$, Mott−Schottky plots were obtained in 0.5 M $Na_2SO_4$ solution (Figure S6b). From the Mott−Schottky plot, the flat band positions of g-$C_3N_4$ and $C_3N_5$ were found to be −1.05 and −0.91 V vs Ag/AgCl, respectively, which can be considered the conduction band position if the Fermi level lies just below conduction band (strong $n$-type character). Using the bandgap values obtained from the Tauc plot (2.65 eV for g-$C_3N_4$ and 1.76 eV for $C_3N_5$), the positions of the valence band edge for g-$C_3N_4$ and $C_3N_5$ were calculated to be +1.60 and +0.85 V vs Ag/AgCl, respectively. Since the standard band edge positions are usually expressed with reference to NHE, the conduction band (CB) and valence band (VB) positions of g-$C_3N_4$ were calculated to −0.85 and +1.80 V vs NHE at pH 0, while CB and VB positions of $C_3N_5$ were found to be −0.72 and +1.04 V vs NHE at pH 0.

XPS valence band spectra of $C_3N_5$ was collected to get further information regarding the band structure (Figure 11a). The intersecting point obtained by extrapolation of XPS VB spectra on $x$ and $y$ axes gave the value of valence band maximum (VB$_{max}$). The VB$_{max}$ of $C_3N_5$ was calculated to be

+0.95 eV, which was approximately the same (+1.04 V) obtained from the Mott−Schottky measurements and UV−vis data. Further, by using XPS VB and optical bandgap (1.76 eV) values, the CB$_{min}$ and VB$_{max}$ of $C_3N_5$ were calculated to be −0.79 and +0.97 eV, while for g-$C_3N_4$, CB$_{min}$ and VB$_{max}$ positions were found to be −0.85 and +1.80 eV, respectively. Figure 11b shows a schematic illustration of the density of states (DOS) distribution in $C_3N_5$ and g-$C_3N_4$.

The dye degradation process begins with the reaction with ·OH radical originating from photogenerated holes in the valence band of the semiconductor. The oxidation potential of water to generate ·OH radical ($H_2O$/·OH) is +2.38 V vs NHE at pH 0, which requires highly oxidative holes. Another route for the generation of ·OH radicals is the reduction of $O_2$ to $O_2^{\bullet-}$ anion radical ($O_2$/$O_2^{\bullet-}$, −0.33 V vs NHE at pH 0) at the conduction band followed by reaction with protons to afford ·OH radicals.[63,65] However, for this process required protons should be derived from water oxidation ($H_2O$/$O_2$, +1.23 V vs NHE at pH 0).[64,66] Unfortunately, the valence band position of $C_3N_5$ is just +1.04 V vs NHE, which cannot facilitate water oxidation thus explaining the absence of photocatalytic activity for MB degradation. Nyquist plots of g-$C_3N_4$ and $C_3N_5$ determined with electrochemical impedance spectroscopy (EIS) under dark and AM1.5G irradiation demonstrate that the semicircle for $C_3N_5$ was larger than for g-$C_3N_4$, which represents a higher charge transfer resistance in $C_3N_5$ compared to g-$C_3N_4$; a higher charge carrier recombination is indicated in $C_3N_5$ (Figure S11).

Because of the unfavorable band edge positions of $C_3N_5$ (CB = −0.72 V and VB = +1.04 V vs NHE at pH 0), it is not able to function as a stand-alone catalyst for the photoelectrochemical splitting of water. However, the excellent visible light absorption of $C_3N_5$ encouraged us to investigate the photosensitizing effect of $C_3N_5$ to increase the photocatalytic performance of $TiO_2$ (a wide bandgap semiconductor).[67] The conduction band of $C_3N_5$ (−0.72 V vs NHE) was more negative than the conduction band of $TiO_2$ (−0.1 V vs NHE), which favors transfer of photogenerated electrons in the CB of $C_3N_5$ to the CB of $TiO_2$.[68] To measure photosensitizing performance, $C_3N_5$ and g-$C_3N_4$ powders were mixed with $TiO_2$ nanoparticles in $\alpha$-terpineol solution (film-forming agent) followed by drop-casting on FTO:glass substrates coated with a thin (∼ 50 nm) blocking layer of $TiO_2$. A three electrode setup consisting of the samples as the photoanode (working electrode), Pt as cathode (counter electrode) and Ag/AgCl reference electrode was used for photoelectrochemical water splitting experiments in 0.1 M $Na_2SO_4$ electrolyte, while a Class A solar simulator was used as the source of AM1.5G simulated sunlight (100 mW cm$^{-2}$). Linear sweep voltammograms of electrodes consisting of $C_3N_5$ and pristine g-$C_3N_4$ samples mixed with $TiO_2$ NPs are shown in Figure 11c. It can be seen from Figure 11c that the photocurrent density for $C_3N_5$ sensitized $TiO_2$ was much higher than g-$C_3N_4$ sensitized $TiO_2$. The current density for $C_3N_5$ and g-$C_3N_4$ sample blended $TiO_2$ sample was found to be 152 and 100 $\mu$A cm$^{-2}$ at an applied potential of +0.6 V vs Ag/AgCl (or 1.23 V vs NHE). To probe the improved photosensitizing performance in the visible region, on−off experiments using a 450 nm LED (54.15 mW cm$^{-2}$) were carried out, which clearly show the alternate drop and rise in photocurrents in on−off cycles (Figure 11d). Figure 11d also shows that the magnitude of the photocurrent was higher for the $C_3N_5$ sample. A similar pattern in the on−off cycle was
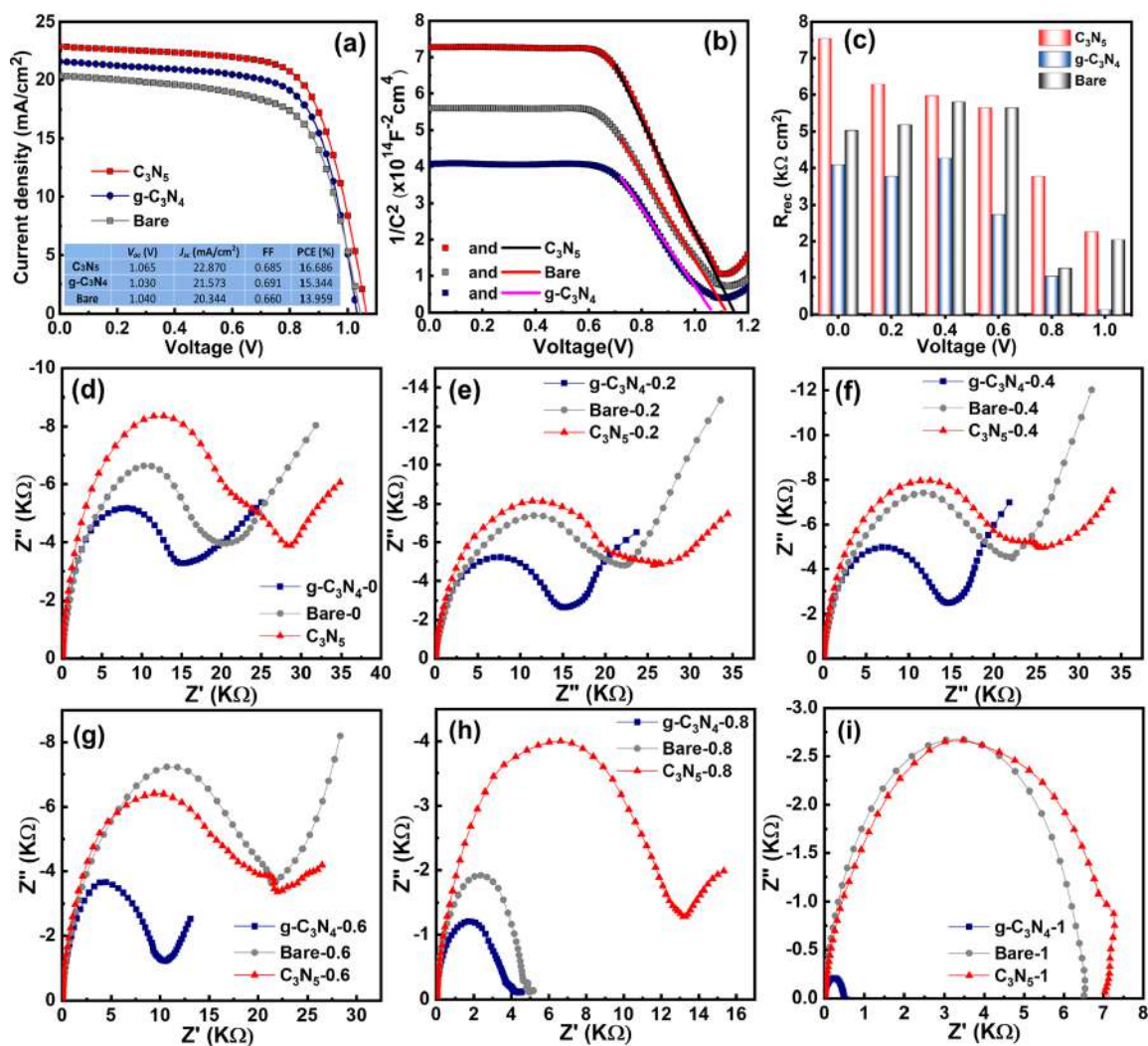
**Figure 12.** (a) Current−voltage characteristics of perovskite solar cells made with bare PbX$_2$, 4 wt % of g-C$_3$N$_4$ and C$_3$N$_5$ under AM1.5 G one sun illumination. (b) Mott−Schottky plot of the perovskite solar cells based undoped and g-C$_3$N$_4$/C$_3$N$_5$-doped perovskite active layers. (c) Recombination resistance of perovskite solar cell based on undoped and doped Perovskite layer with CN and MHP in dark conditions. The corresponding equivalent circuit is shown in insets where $R_s$ is series resistance, $C$ is high-frequency capacitance, $R$ is recombination resistance and $Q$ is a constant phase element (CPE) with coefficient $N$. (d−i) Nyquist plots for perovskite solar cells made with bare PbX$_2$, g-C$_3$N$_4$ and C$_3$N$_5$ doping under dark conditions at 0.0, 0.2, 0.4, 0.6, 0.8 and 1.0 V.

observed when samples were irradiated with 505 nm LED (40.48 mW cm$^{-2}$), confirming the improved photosensitizing properties of C$_3$N$_5$ at longer wavelengths (Figure S12). Further, photoelectrochemical water splitting experiment carried out using Na$_2$S (2.0 mmol) as hole scavenger showed enhanced photocurrent density, reaching up to 465 $\mu$A cm$^{-2}$ for C$_3$N$_5$ under AM 1.5 G irradiation (>420 nm) (Figure S13). Under identical conditions, the value of photocurrent density for g-C$_3$N$_4$ was found to be 373 $\mu$A cm$^{-2}$ (Figure S13a). A similar pattern was followed at higher wavelengths and calculated current density for C$_3$N$_5$ was found to be 454 and 145 $\mu$A cm$^{-2}$ at 450 and 505 nm, while for g-C$_3$N$_4$ the value of current density was found to be 275 and 80 $\mu$A cm$^{-2}$, respectively (Figure S13b). Photocurrent response of C$_3$N$_5$ as a function of time during light on−off cycle does not change significantly compared to g-C$_3$N$_4$, which demonstrates resiliency of C$_3$N$_5$ under reaction conditions and charge flow (Figure S14). The maximum applied bias photon-to-current efficiency (ABPE) and incident photon-to-current efficiency (IPCE) achieved by C$_3$N$_5$ was 0.059 and 2.33% (at 450 nm),

while the value for g-C$_3$N$_4$ was 0.048 and 1.41% (at 450 nm), respectively (Figure S13c,d).

To demonstrate the optoelectronic application of our newly synthesized graphenic semiconductor, we employed C$_3$N$_5$ as the electron transport layer (ETL) in MAPbBr$_3$ (CH$_3$NH$_3$PbBr$_3$) based perovskite solar cells and obtained a good result. Carbon based materials have frequently been used as hole transport layers (HTLs) or hole collection electrodes in MAPbBr$_3$ based solar cells, but have almost never been used (effectively) as ETLs to boost the open circuit photovoltage. Using C$_3$N$_5$ as the ETL and with no optimization of any kind, we measured a $V_{oc}$ of 1.3 V, $J_{sc}$ of 7.5 mA cm$^{-2}$ and a FF (fill factor) of 0.4 to obtain a power conversion efficiency (PCE) of 4.2% (Figures S15 and S16 in Supporting Information). Some context is needed to appreciate the significance of the aforementioned result. Methylammonium lead bromide (MAPbBr$_3$) is a halide perovskite with an electronic bandgap of 2.23 eV, which has two major advantages for solar cell applications in comparison to the more commonly used methylammonium lead iodide (MAPbI$_3$, CH$_3$NH$_3$PbI$_3$). In

**Table 4. Photovoltaic Performance of HPSCs Made with Bare PbX$_2$, 4 wt % g-C$_3$N$_4$ and C$_3$N$_5$ in PbX$_2$ Solution under AM1.5 G Solar Simulated Light**

| | | $V_{oc}$ (V) | $J_{sc}$ (mA/cm$^2$) | FF | PCE (%) |
|---|---|---|---|---|---|
| C$_3$N$_5$ | maximum | 1.065 | 22.870 | 0.685 | 16.686 |
| | average | 1.026 ± 0.043 | 22.560 ± 1.039 | 0.654 ± 0.044 | 15.142 ± 1.442 |
| g-C$_3$N$_4$ | maximum | 1.030 | 21.573 | 0.691 | 15.344 |
| | average | 0.984 ± 0.042 | 21.204 ± 0.565 | 0.670 ± 0.017 | 13.981 ± 0.949 |
| bare | maximum | 1.040 | 20.344 | 0.660 | 13.959 |
| | average | 1.041 ± 0.035 | 20.394 ± 0.200 | 0.647 ± 0.020 | 13.713 ± 0.245 |

theory, it enables the construction of much higher $V_{oc}$ solar cells that can be used to power electrocatalytic and electrochemical reactions and second, MAPbBr$_3$ is known to have superior ambient stability (less moisture sensitivity) and operational stability (due to the absence of phase transitions and enhanced thermal stability at a high working temperature) compared to MAPbI$_3$.[69] However, until recently, most works in this area failed to achieve the expected high $V_{oc}$ value, and the typical $V_{oc}$ values obtained using were in the range 0.90–1.16 V.[70] The use of carbon based charge transport layers has enabled a dramatic improvement in the performance of MAPbBr$_3$ based photovoltaic devices by generating photovoltages in excess of 1.3 V (as high as 1.6 V) without suffering a corresponding penalty in the short circuit current ($J_{sc}$). The first such report was by Wu et al.[71] wherein indene-C60 bisadduct (ICBA) was used as the acceptor in conjunction with MAPbBr$_3$ to realize a high $V_{oc}$ perovskite solar cell. Shortly thereafter, Li et al. used carbon nanotubes as an efficient hole collector for MAPbBr$_3$ solar cells and achieved a $V_{oc}$ of 1.4 V.[72] MAPbBr$_3$ sandwiched between modified PEDOT:PSS (hole transport layer) and PC$_{61}$BM (electron transport layer) resulted in a solar cell with a $V_{oc}$ of 1.52 V[73] while a graphitic carbon anode (with no hole transport layer) and TiO$_2$ electron transport layer were used by Liang et al. to realize a MAPbBr$_3$ solar cell with a $V_{oc}$ as high as 1.57 V.[74]

The origin of the poor $V_{oc}$ values was poorly understood for a long time. Even now, there are two distinct explanations: one based on active layer material quality issues and another based on high interfacial recombination. For instance, vapor deposited MAPbBr$_3$ films were found to generate high $V_{oc}$ values in comparison with solution-deposited films, which was attributed to the superior morphology and grain size in the vapor deposited films, and supported the explanation based invoking material quality.[75] The second explanation was supported by the observation of high $V_{oc}$ values when hole transport layers with deep HOMO levels were used, indicating that the separation of the electron- and hole- quasi-Fermi levels at the charge extraction interfaces was the controlling mechanism determining $V_{oc}$.[76] Our examination of MAPbBr$_3$ solar cells using C$_3$N$_5$ as the ETL provides a way to reconcile the above explanations. On the one hand, the high CB position of C$_3$N$_5$ is better aligned with the CB of MAPbBr$_3$, and enables an optimal value for the electron quasi-Fermi level at the perovskite–C$_3$N$_5$ interface. On the other hand, the low dark current observed using C$_3$N$_5$ ETL in comparison to both TiO$_2$ and g-C$_3$N$_4$ ETLs (Figure S17 in Supporting Information) indicates suppression of trap-mediated hopping through MAPbBr$_3$ due to the insertion of C$_3$N$_5$ as a midgap state-free barrier layer, thus enabling the circumventing of active layer material quality issues. In summary, it is noteworthy that an unoptimized ETL made with a brand new semiconductor (C$_3$N$_5$) that was cast into films from a particulate suspension,

generated a $V_{oc}$ value of 1.3 V, higher than that generated by TiO$_2$ and g-C$_3$N$_4$ ETLs.

The photovoltaic performance of halide perovskite solar cells is highly dependent on grain size and defect free lattice states and presence of small number of defect and trap sites have a detrimental effect. The trap assisted recombinations can be minimized by passivating perovskite layer with graphenic materials due to their high carrier mobility and surface area, which can efficiently capture charge and improve transportation behavior resulting in better photoconversion efficiency.[77] Further, incorporation of graphenic semiconductors with perovskite precursor provide crystallization surface, which helps in increasing of grain size and minimize defects density at grain boundaries. The increased conjugation in C$_3$N$_5$ should lead to electron-rich conductive surface with high charge carrier density and better carrier mobility than g-C$_3$N$_4$. To verify this assumption, we have blended MA$_x$FA$_{1-x}$Pb-(I$_{0.85}$Br$_{0.15}$)$_3$ based perovskite with different wt % of C$_3$N$_5$ and g-C$_3$N$_4$. Under optimized conditions, 4 wt % doping of g-C$_3$N$_4$ and C$_3$N$_5$ with respect to PbX$_2$ was found to perform best and C$_3$N$_5$ outperformed g-C$_3$N$_4$ and bare PbX$_2$ based solar cell architecture attributed to better charge separation in more conjugated C$_3$N$_5$ scaffold and reduced trap sites.

Figure 12a shows the $J-V$ curves of the best performing solar cells devices based on undoped and doped perovskite layers while the photovoltaic performance of solar cells is summarized in Table 4. Solar cells made with a compact undoped perovskite solar cell yielded a short circuit current density ($J_{sc}$) of about 20.344 mA/cm$^2$, an open circuit voltage ($V_{oc}$) of 1.04 V and fill factor (FF) of about 66% resulting in the overall power conversion efficiency (PCE) of about 13.959%. While, solar cell made with g-C$_3$N$_4$-doped perovskite layer show a $J_{sc}$ of 21.573 mA/cm$^2$, $V_{oc}$ of 1.03 V and fill factor of about 69.1% and corresponding PCE of about 15.344%. C$_3$N$_5$-doped perovskite solar cells displayed a PCE value of 16.686% resulting from $V_{oc}$ of 1.065 V, $J_{sc}$ of 22.87 mA/cm$^2$ and FF of 68.5%.

Capacitance–voltage measurement on fabricated devices with doped/undoped perovskite layer was measured at 10 kHz frequency in dark to determine bulk properties such as doping density ($N_D$) and energy equilibrium at the contacts, which is related to the flat-band potential ($V_{fb}$).[78] Mott–Schottky plots for the devices made with doped and undoped perovskite layer are shown in Figure 12b.

$$\frac{1}{C_{sc}^2} = \frac{2}{e\varepsilon_0\varepsilon_r N_D}\left\{(V - V_{FB}) - \frac{kT}{e}\right\} \tag{8}$$

$$N_D = \frac{2}{e\varepsilon_0\varepsilon_r n} \tag{9}$$

$V_{fb}$ and $N_D$ were calculated by using eq 8 and eq 9 respectively, where $C_{sc}$ is the space-charge capacitance (i.e.,
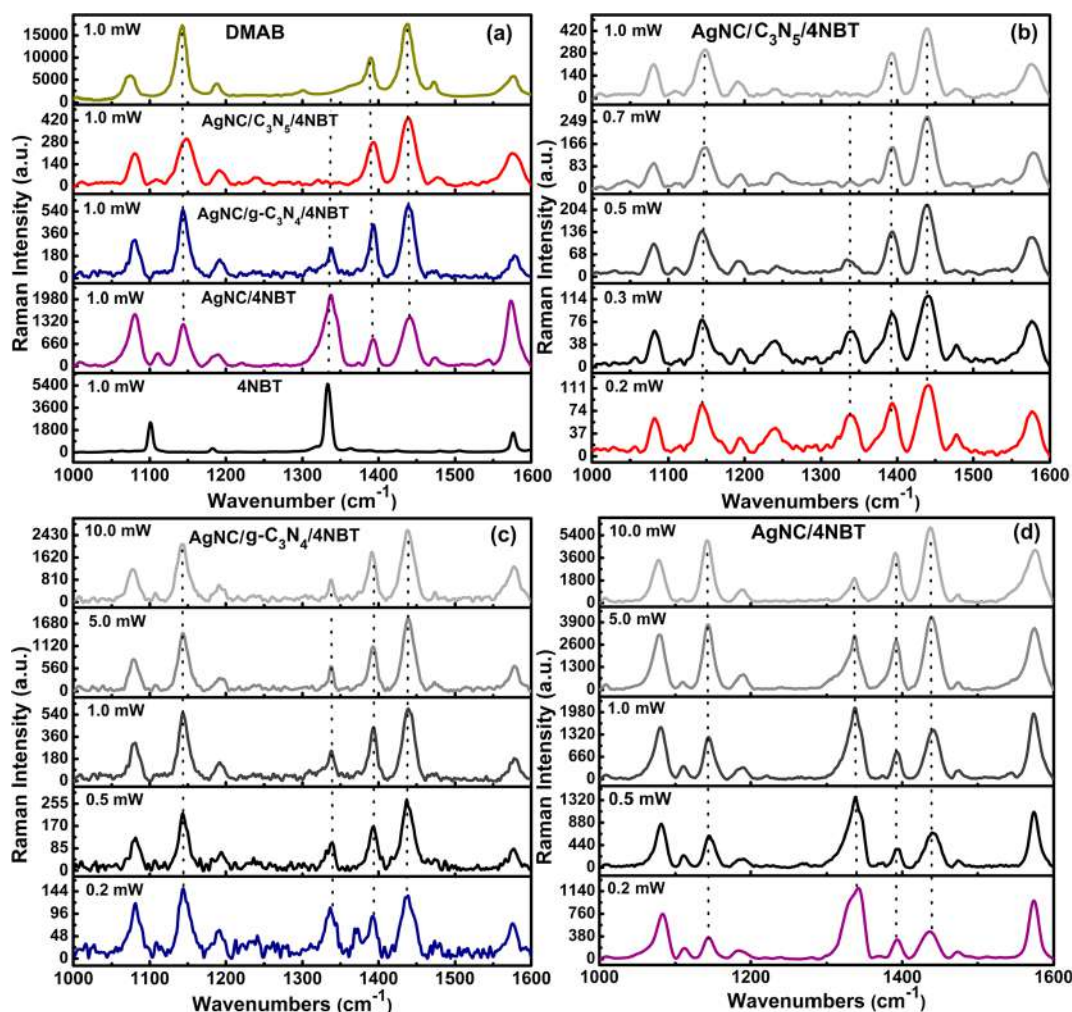
**Figure 13.** (a) Raman spectrum of pristine 4NBT (black), DMAB (yellow) and comparison of SERS spectra of plasmon-exciton coinduced surface catalytic reaction of 4NBT to DMAB on AgNC (purple), AgNC/g-$C_3N_4$ (blue) and AgNC/$C_3N_5$ (red) under 532 nm laser irradiation at 1.0 mW power and 60 s accumulation time and SERS spectra as a function of laser power for plasmon-exciton coinduced surface catalytic transformation of 4NBT to DMAB on (b) AgNC/$C_3N_5$ (c) AgNC/g-$C_3N_4$ and (d) AgNC. The gradual lightening of color as a function of laser power represents the transformation of 4NBT to DMAB.

film capacitance) per unit area; $\varepsilon_r$ is the dielectric constant of the material, $\varepsilon_0$ is the vacuum permittivity, $k$ is Boltzmann constant, $T$ is temperature in Kelvin, $e$ is the electron charge and $V$ is the applied potential. The measured $V_{fb}$ of bare undoped, g-$C_3N_4$-doped and $C_3N_5$-doped perovskite solar cell was found to be 1.12, 1.08, and 1.15 V respectively, while carrier concentration of the respective devices was found to be $1.74 \times 10^{16}$, $1.96 \times 10^{16}$ and $1.36 \times 10^{16}$ cm$^{-3}$. This proves that doping perovskite layer with $C_3N_5$ significantly improves the charge transport in the device compared to the undoped and g-$C_3N_4$-doped devices.

To explore the charge transport characteristics, hole only devices with the architecture of FTO/PEDOT:PSS/Perovskite/Spiro-oMeTAD/Au was measured by the space charge limited current (SSLC) model described by the following equation:

$$J = \frac{9}{8L^3}\epsilon_0\epsilon_r\mu V^2 \tag{10}$$

Where $\epsilon_0$, $\epsilon_r$, $\mu$ and $L$ are permittivity of the free space, relative permittivity of the perovskite, carrier mobility in the perovskite layer and thickness of perovskite layer, respectively. The hole

mobility in pure perovskite was found to be $2.55 \times 10^{-3}$ cm$^2$/(V s), while that of g-$C_3N_4$- and $C_3N_5$-doped perovskite was found to be $3.28 \times 10^{-3}$ cm$^2$/(V s) and $4.33 \times 10^{-3}$ cm$^2$/(V s), respectively (Figure S19).

To get insight into the charge transfer properties of perovskite solar cells based on undoped and doped perovskite layer, solid-state impedance spectroscopy measurements in the frequency range from 0.1 Hz to 1 MHz at different applied bias under dark conditions were performed. The resulting Nyquist plots were fitted with the circuit shown in inset of Figure 12c, where $R_s$ is series resistance, $R_{rec}$ and $C$ represent the resistance and capacitance at the interface between the active layer and charge transport layer and $Q$ is a constant phase element (CPE) with coefficient $N$. The resulting recombination resistance of different solar cells obtained after fitting the Nyquist plot observed from the low-frequency region at different voltages is shown in Figure 12d−i. The $C_3N_5$-doped device showed a higher value of $R_{rec}$ compared to the g-$C_3N_4$-doped and undoped devices. As the electron and hole transporting layers for all kind of devices are the same, the difference in $R_{rec}$ is mostly governed by the change in the interfacial property of perovskite layer induced by doping with
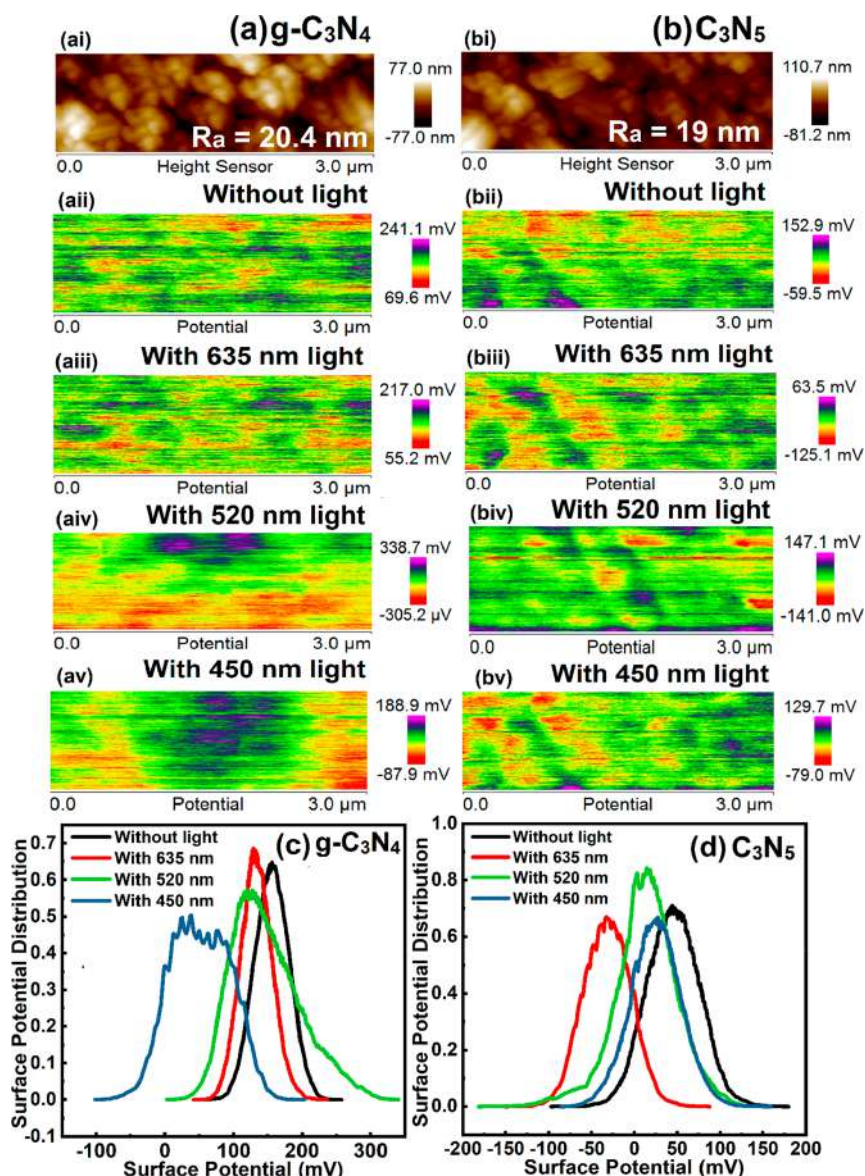
**Figure 14.** (a and b) Topographical AFM images (ai, bi) and Surface potential maps of g-C$_3$N$_4$ and C$_3$N$_5$ samples deposited on FTO (aii and bii) without light, (aiii and biii) with 635 nm lased, (aiv and biv) with 520 nm laser, (av and bv) with 450 nm laser in sequence of top to bottom and surface potential distribution of (c) g-C$_3$N$_4$ and (d) C$_3$N$_5$ samples deposited on FTO under dark conditions, under illumination with 635, 520 and 450 nm laser.

C$_3$N$_5$ and g-C$_3$N$_4$. Interfacial recombination is inversely proportional to the recombination resistance; therefore, it can be concluded that the interfacial charge recombination in perovskite solar cells significantly gets suppressed by doping with MHP, while it increases by doping with g-C$_3$N$_4$ resulting in an improved $V_{oc}$ in C$_3$N$_5$ based device followed by the undoped and doped devices.

The low band gap and extended $\pi$ conjugation of C$_3$N$_5$ makes it an excellent candidate to harvest solar light to drive visible light induced catalytic reaction. Recently, plasmonic materials capable of generating hot electrons, coupled with graphenic materials, have shown wide potential in plasmon-exciton coinduced surface catalytic reactions.[79] The plasmon-exciton coupling for codriven chemical reactions can be measured by surface enhanced Raman spectroscopy (SERS).[80] To probe the viability C$_3$N$_5$ for promoting chemical reaction on its surface, the transformation of 4NBT (4-nitrobenzene-thiol) to DMAB (4,4′-dimercaptoazobenzene) was chosen as

model reaction, while silver nanocubes (AgNC)[81] were used as plasmonic material. The comparative SERS spectra of NBT adsorbed on bare AgNC, and AgNC decorated on g-C$_3$N$_4$ and C$_3$N$_5$ using 532 nm laser and 1 mW laser power are presented in Figure 13a. Normal Raman spectra of the pristine 4NBT powder show three main Raman signals at 1101, 1332 and 1576 cm$^{-1}$ assigned to S—C stretch, NO$_2$ vibration and C=C stretch, respectively.[82] After irradiating with 532 nm laser with a 1 mW power intensity, the N—O vibration was decreased and new peaks at 1142 (C—N stretch), 1389 and 1438 (N=N stretch) cm$^{-1}$ corresponded to DMAB a$_g$ modes emerged demonstrating conversion of 4NBT to DMAB.[83] For bare AgNC the drop in 4NBT peak was not significant, which showed inefficient surface-plasmon-to-hot-electron conversion to promote plasmon-driven chemical reaction. The AgNC/g-C$_3$N$_4$ showed a slight lowering of 4NBT peak intensity and rise in DMAB peaks; however, the peak did not disappear suggesting incomplete transformation at lower laser power.

While for AgNC/$C_3N_5$ the N—O vibration peak completely disappeared at 1.0 mW laser power. Further, we tested laser power dependent SERS spectra on NBT adsorbed samples, which demonstrate complete disappearance of 4NBT peaks for Ag/$C_3N_5$ even at 0.7 mW, while bare Ag and AgNC/g-$C_3N_4$ system could not achieve complete degradation even at 10 mW laser power (Figure 13b−d). Magnified SERS spectra of Ag/$C_3N_5$ in the 1270−1470 cm$^{-1}$ region showed a gradual decrease in N—O vibration peak as a function of laser power AgNC and completely disappeared at 1.0 mW (Figure S20). A sluggish transformation rate was observed for AgNC/g-$C_3N_4$ and AgNC as evident from the increase in 4NBT peak at 1332 cm$^{-1}$ along with DMAB peak at 1389 and 1438 cm$^{-1}$ as a function of laser intensity. The excellent conversion efficiency of AgNC/$C_3N_5$ assembly was attributed due to better plasmon-to-electron conversion efficiency on conjugated $C_3N_5$'s surface, which lead to high-density hot electrons to facilitate high catalytic conversion.[79b]

We performed thermogravimetric analysis (TGA) analysis of g-$C_3N_4$ and $C_3N_5$ samples to determine the thermal stability of materials (Figure S21). The TGA thermogram of g-$C_3N_4$ shows two weight loss regimes in the range of 60−150 °C and 500−740 °C (Figure S21a). The first small weight loss (∼6%) in the range of 60−150 °C was due to loss of surface adsorbed water molecules. The second major weight loss started from 550 °C, showed slow weight loss (∼8%) up to 635 °C due to loss of $NH_2$ and condensation of heptazine units followed by almost ∼70% sharp weight loss in the range of 635−740 °C due to degradation of heptazine moieties.[84] Following that, a steady weight loss was observed up to 900 °C due to the removal of residual carbon material. For $C_3N_5$, an initial small weight loss of 6% in the range of 60−150 °C was attributed due to loss of surface adsorbed and intercalated water (Figure S21b). A second steady weight loss (∼34%) observed in the temperature range of 420−630 °C was assigned to loss of bridging azo nitrogens (−N═N−) and edge decorated −$NH_2$ nitrogens. The absence of any sharp weight loss for azo nitrogens demonstrates that azo nitrogens were not localized but present in a cross-linked heptazine network. Previous reports on azo-linked polymer also demonstrated excellent thermal stability of such polymers due to the formation of a rigid structure.[85] Further, the observed weight loss value was in close agreement with expected weight loss value for azo nitrogen (33.5%) calculated by considering removal of three azo nitrogens (−N═N− shared by two heptazine) from azo-bridged $C_6N_{10}$ unit, leaving behind $C_6N_7$ heptazine unit. These results further validated the presence of azo nitrogens in $C_3N_5$ polymer. Approximately 38% sharp weight loss in 630−720 °C region was assigned to degradation of heptazine ring system followed by slow weight loss up to 900 °C for residual carbon. Further, to investigate the nature of the product formed at high temperature, we annealed the sample in a closed evacuated quartz tube at 800 °C for 4 h. The orange product turned black and stuck to the wall of the tubes. Raman analysis of the product showed specific D, G band along with the 2D band and demonstrate its transformation into N-doped graphene/carbon (Figure S22). Previous reports also demonstrate the transformation of carbon nitride based materials/nitrogenous precursors into N-graphene/N-carbon at higher temperatures.

To understand charge carrier dynamics and recombination mechanisms in $C_3N_5$, the surface potential changes of the samples under dark and laser illumination at different wavelengths, were measured using Kelvin Probe Force Microscopy (KPFM) as illustrated in Figure 14. The surface topographical AFM image of g-$C_3N_4$ and $C_3N_5$ thin films deposited on bare FTO reveals an average roughness of 20.4 and 19 nm, respectively (Figure 14ai,bi). Figure 14aii−v and bii−v displays the surface potential map of g-$C_3N_4$ and $C_3N_5$ samples under dark conditions, 635, 520 and 450 nm, respectively. The FTO was grounded and behaves as an electron sink for photogenerated charges, leaving holes behind. The surface potential map under dark for both g-$C_3N_4$ and $C_3N_5$ shows even distribution of charge all over the surface of samples, (Figure 14aii,bii). After illumination with 635 nm laser the contrast of blue spots (positive potential shift) in the surface potential map was increased for both g-$C_3N_4$ and $C_3N_5$; however, this change was much intense for $C_3N_5$. Under 520 nm light, the density of blue spots was slightly higher for g-$C_3N_4$ than $C_3N_5$, which drastically increased under 450 nm illumination (Figure 14a (aiv,v) and Figure 14b (biv,v). These observations demonstrate that highest charge generation and accumulation on the surface was at 450 nm for g-$C_3N_4$ and at 635 nm for $C_3N_5$ while remaining moderate for both at 520 nm. Further, values of surface potential measured by KPFM under dark condition were found to be +156 and +45 mV for g-$C_3N_4$ and $C_3N_5$ respectively, which agreed well with the increased electron density on $C_3N_5$ than g-$C_3N_4$ due to contribution of charge from azo motif to heptazine ring system via extended orbital overlap (Figure 14c,d). The high surface negative charge of $C_3N_5$ was also confirmed by ζ-potential measurements (Figure S8). After illumination with 450 nm light, the surface potential was negatively shifted reaching maximum +40 mV for g-$C_3N_4$ and +25 mV for $C_3N_5$. Higher change in contact potential difference (CPD) or SP, i.e. 102 mV, for g-$C_3N_4$ was observed due to good absorption at 450 nm for generation of electron−hole pairs and accumulation of negative charge on the sample surface. The broad surface potential peaks and significantly larger CPD shift for g-$C_3N_4$ were attributed possibly due to the longer lifetime (as confirmed by TRPL, Figure 8a) of g-$C_3N_4$ charge carriers resulting into delayed recombination of accumulated charge. Under 520 nm illumination, the surface potential values for g-$C_3N_4$ and $C_3N_5$ were measured to be 123 and 8 mV, while the change in SP was found to be 33 and 37 mV, respectively. For g-$C_3N_4$, relatively small CPD shifting at 520 nm can be explained due to its limited absorption at 520 nm wavelength generating fewer numbers of excitons, while in $C_3N_5$ most of the photogenerated charge get recombined due to faster recombination rate. Interestingly, $C_3N_5$ showed an unusually high SP shift (77 mV) at 635 nm, while g-$C_3N_4$ showed an explicitly small CPD shift (30 mV). The exceptional high SP shift at 635 nm demonstrated azo motif plays a certain role in charge carrier generation and stabilization at a longer wavelength. Azo-bridged aromatic compounds are well-known for their visible light absorption due to the presence of azo chromophore (−N═N−) in conjugation with aromatic units. The n−π* transition corresponding to azo nitrogen nonbonding orbital to the π* orbital of conjugated nitrogens in azo moiety occurs at low energy giving visible light absorption.[86] In $C_3N_5$ where electron withdrawing heptazine units ($C_6H_7$) were bridged together with azo bonds, these low energy transition can take place at 635 nm resulting into increase CPD shift at 635 nm. The high surface potential of $C_3N_5$ at 635 nm validates its potential to generate excitons at longer wavelengths.

## CONCLUSION

We report the synthesis of a modified carbon nitride framework $C_3N_5$ polymer containing exceptionally high N:C atomic ratio (5:3) using melem hydrazine as the monomeric unit. Extensive characterization of $C_3N_5$ with XPS, EELS, NMR spectroscopy and elemental analysis suggested the presence of heptazine moiety bridged by azo nitrogens in the $C_3N_5$ framework. Because of the overlap between the $\pi$ orbitals of azo-bridged units and the $\pi$-conjugated network of the heptazine unit, the bandgap of $C_3N_5$ material was significantly reduced which, in turn, enabled optical absorption extended up to 700 nm and a bandgap of 1.76 eV. The position of the valence band in $C_3N_5$ was raised (+1.04 V vs NHE) in comparison to g-$C_3N_4$ (+1.80 V vs NHE) and $C_3N_5$ displayed excellent photosensitizing behavior to sensitize $TiO_2$ at longer wavelengths (505 nm) to facilitate photoelectrochemical water splitting. Because of the increased nitrogen content and the availability of electron-rich basic nitrogen sites, $C_3N_5$ materials displayed astonishing dye adsorption performance for methylene blue removal reaching 90% adsorption−desorption equilibria within 1 min and complete adsorption−desorption equilibria within 10 min. In conjunction with Ag nanocubes, $C_3N_5$ displayed excellent photocatalytic activity for the plasmon-exciton (plexciton) codriven reduction of 4-nitrobenzenethiol to 4,4′-dimercaptoazobenzene. A prototypical solar cell device using $C_3N_5$ ETL and $MAPbBr_3$ displayed an improved $V_{oc}$ of 1.3 V and power conversion efficiency (PCE) of 4.2% higher than g-$C_3N_4$ ETL. $C_3N_5$ blended with $MA_xFA_{1−x}Pb(I_{0.85}Br_{0.15})_3$ perovskite active layer achieved a photoconversion efficiency (PCE) as high as 16.7%.

## ASSOCIATED CONTENT

### Ⓢ Supporting Information

The Supporting Information is available free of charge on the ACS Publications website at DOI: 10.1021/jacs.9b00144.

> Experimental details, chemical structures, Supporting Figures (Figure S1−S22), XPS, ssNMR, Raman, electrochemical characterization (Mott−Schottky, EIS), PL, fluorescence lifetime imaging, $\zeta$-potential, EELS, TGA, photoelectrochemical water splitting results (under AM 1.5G irradiation, LEDs PCE, IPCE, APCE, $i−t$ curve), solar cell results ($J−V$ curves, action spectra) and plexcitonic performance (SERS spectra) (PDF)

## AUTHOR INFORMATION

### Corresponding Authors

*pawan@ualberta.ca
*kshankar@ualberta.ca

### ORCID Ⓘ

Pawan Kumar: 0000-0003-2804-9298
Guy M. Bernard: 0000-0003-1507-6705
Vladimir K. Michaelis: 0000-0002-6708-7660
Karthik Shankar: 0000-0001-7347-3333

### Notes

The authors declare no competing financial interest.

## ACKNOWLEDGMENTS

## REFERENCES

(1) (a) Brabec, C. J.; Winder, C.; Sariciftci, N. S.; Hummelen, J. C.; Dhanabalan, A.; van Hal, P. A.; Janssen, R. A. *Adv. Funct. Mater.* **2002**, *12*, 709−712. (b) Kim, J.-S.; Lu, L.; Sreearunothai, P.; Seeley, A.; Yim, K.-H.; Petrozza, A.; Murphy, C. E.; Beljonne, D.; Cornil, J.; Friend, R. H. *J. Am. Chem. Soc.* **2008**, *130*, 13120−13131. (c) Liang, Y. Y.; Yu, L. P. *Acc. Chem. Res.* **2010**, *43*, 1227−1236. (d) Bandara, J.; Shankar, K.; Grimes, C. A.; Thelakkat, M. *Thin Solid Films* **2011**, *520*, 582−590. (e) Baeg, K. J.; Caironi, M.; Noh, Y. Y. *Adv. Mater.* **2013**, *25*, 4210−4244. (f) Hu, X. W.; Dong, Y.; Huang, F.; Gong, X.; Cao, Y. J. *J. Phys. Chem. C* **2013**, *117*, 6537−6543. (g) Scaccabarozzi, A.; Stingelin, N. J. *J. Mater. Chem. A* **2014**, *2*, 10818−10824. (h) Fokina, A.; Lee, Y.; Chang, J. H.; Park, M.; Sung, Y.; Bae, W. K.; Char, K.; Lee, C.; Zentel, R. *Adv. Mater. Interfaces* **2016**, *3*, 1600279. (i) Gao, L.; Zhang, Z. G.; Bin, H.; Xue, L.; Yang, Y.; Wang, C.; Liu, F.; Russell, T. P.; Li, Y. *Adv. Mater.* **2016**, *28*, 8288−8295. (j) Mola, G. T.; Dlamini, W. E.; Oseni, S. O. *J. Mater. Sci.: Mater. Electron.* **2016**, *27*, 11628−11633. (k) Chang, P.-H.; Tsai, Y.-C.; Shen, S.-W.; Liu, S.-Y.; Huang, K.-Y.; Li, C.-S.; Chang, H.-P.; Wu, C.-I. *ACS Photonics* **2017**, *4*, 2335−2344. (l) Schroeder, B. C.; Kurosawa, T.; Fu, T. R.; Chiu, Y. C.; Mun, J.; Wang, G. J. N.; Gu, X. D.; Shaw, L.; Kneller, J. W. E.; Kreouzis, T.; Toney, M. F.; Bao, Z. A. *Adv. Funct. Mater.* **2017**, *27*, 1701973. (m) Zhao, W.; Li, S.; Zhang, S.; Liu, X.; Hou, J. *Adv. Mater.* **2017**, *29*, 1604059. (n) Kang, M. J.; Khim, D.; Kim, J.; Lee, H. J.; Jo, J. Y.; Baeg, K. J.; Kim, D. Y. *Org. Electron.* **2018**, *58*, 12−17. (o) Brabec, C. J.; Winder, C.; Sariciftci, N. S.; Hummelen, J. C.; Dhanabalan, A.; van Hal, P. A.; Janssen, R. A. J. *Adv. Funct. Mater.* **2002**, *12*, 709−712. (p) Kim, J. S.; Lu, L.; Sreearunothai, P.; Seeley, A.; Yim, K. H.; Petrozza, A.; Murphy, C. E.; Beljonne, D.; Cornil, J.; Friend, R. H. *J. Am. Chem. Soc.* **2008**, *130*, 13120−13131. (q) Bandara, J.; Shankar, K.; Grimes, C. A.; Thelakkat, M. *Thin Solid Films* **2011**, *520*, 582−590. (r) Scaccabarozzi, A. D.; Stingelin, N. J. *J. Mater. Chem. A* **2014**, *2*, 10818−10824. (s) Gao, L.; Zhang, Z. G.; Bin, H. J.; Xue, L. W.; Yang, Y. K.; Wang, C.; Liu, F.; Russell, T. P.; Li, Y. F. *Adv. Mater.* **2016**, *28*, 8288−8295. (t) Chang, P. H.; Tsai, Y. C.; Shen, S. W.; Liu, S. Y.; Huang, K. Y.; Li, C. S.; Chang, H. P.; Wu, C. I. *ACS Photonics* **2017**, *4*, 2335−2344. (u) Zhong, L.; Gao, L.; Bin, H. J.; Hu, Q.; Zhang, Z. G.; Liu, F.; Russell, T. P.; Zhang, Z. J.; Li, Y. F. *Adv. Energy Mater.* **2017**, *7*, 1602215.

(2) Po, R.; Bianchi, G.; Carbonera, C.; Pellegrino, A. *Macromolecules* **2015**, *48*, 453−461.

(3) (a) Di Pietro, R.; Fazzi, D.; Kehoe, T. B.; Sirringhaus, H. *J. Am. Chem. Soc.* **2012**, *134*, 14877−14889. (b) Chen, C. Y.; Tsao, C. S.; Huang, Y. C.; Liu, H. W.; Chiu, W. Y.; Chuang, C. M.; Jeng, U. S.; Su, C. J.; Wu, W. R.; Su, W. F.; Wang, L. *Nanoscale* **2013**, *5*, 7629−7638. (c) Phan, H.; Wang, M.; Bazan, G. C.; Nguyen, T. Q. *Adv. Mater.* **2015**, *27*, 7004−7009. (d) Ye, Z.; Cui, H.; Yang, X.; Qiu, F. *J. Mater. Chem. C* **2015**, *3*, 1949−1956. (e) Pearson, A. J.; Hopkinson, P. E.; Couderc, E.; Domanski, K.; Abdi-Jalebi, M.; Greenham, N. C. *Org. Electron.* **2016**, *30*, 225−236. (f) Hsieh, Y. J.; Huang, Y. C.; Liu, W. S.; Su, Y. A.; Tsao, C. S.; Rwei, S. P.; Wang, L. *ACS Appl. Mater. Interfaces* **2017**, *9*, 14808−14816. (g) Un, H. I.; Zheng, Y. Q.; Shi, K.; Wang, J.

Y.; Pei, J. *Adv. Funct. Mater.* **2017**, *27*, 1605058. (h) Di Pietro, R.; Fazzi, D.; Kehoe, T. B.; Sirringhaus, H. *J. Am. Chem. Soc.* **2012**, *134*, 14877−14889. (i) Kim, S. H.; Yoon, W. M.; Jang, M.; Yang, H.; Park, J. J.; Park, C. E. *J. Mater. Chem.* **2012**, *22*, 7731−7738. (j) Phan, H.; Wang, M.; Bazan, G. C.; Nguyen, T. Q. *Adv. Mater.* **2015**, *27*, 7004−7004. (k) Ye, Z.; Cui, H. N.; Yang, X. B.; Qiu, F. *J. Mater. Chem. C* **2015**, *3*, 1949−1956. (l) Pearson, A. J.; Hopkinson, P. E.; Couderc, E.; Domanski, K.; Abdi-Jalebi, M.; Greenham, N. C. *Org. Electron.* **2016**, *30*, 225−236. (m) Un, H. I.; Zheng, Y. Q.; Shi, K.; Wang, J. Y.; Pei, J. *Adv. Funct. Mater.* **2017**, *27*, 1605058.

(4) (a) Matthews, J. R.; Niu, W. J.; Tandia, A.; Wallace, A. L.; Hu, J. Y.; Lee, W. Y.; Giri, G.; Mannsfeld, S. C. B.; Xie, Y. T.; Cai, S. C.; Fong, H. H.; Bao, Z. N.; He, M. Q. *Chem. Mater.* **2013**, *25*, 782−789. (b) Marzano, G.; Ciasca, C. V.; Babudri, F.; Bianchi, G.; Pellegrino, A.; Po, R.; Farinola, G. M. *Eur. J. Org. Chem.* **2014**, *2014*, 6583−6614. (c) Bohra, H.; Wang, M. F. *J. Mater. Chem. A* **2017**, *5*, 11550−11571.

(5) (a) Zhang, X. M.; Wang, A. Z.; Zhao, M. W. *Carbon* **2015**, *84*, 1−8. (b) Berger, D.; Ratsch, C. *Phys. Rev. B: Condens. Matter Mater. Phys.* **2016**, *93*, 235441.

(6) (a) Kumar, P.; Boukherroub, R.; Shankar, K. *J. Mater. Chem. A* **2018**, *6*, 12876−12931. (b) Linley, S.; Liu, Y.; Ptacek, C. J.; Blowes, D. W.; Gu, F. X. *ACS Appl. Mater. Interfaces* **2014**, *6*, 4658−4668. (c) Putz, M. V.; Buzatu, D. L.; Mirica, M. C.; Ori, O. *Fullerenes, Nanotubes, Carbon Nanostruct.* **2018**, *26*, 303−314.

(7) (a) Sridharan, K.; Kuriakose, T.; Philip, R.; Park, T. J. *Appl. Surf. Sci.* **2014**, *308*, 139−147. (b) Liu, J.; Liu, Y.; Liu, N.; Han, Y.; Zhang, X.; Huang, H.; Lifshitz, Y.; Lee, S.-T.; Zhong, J.; Kang, Z. *Science* **2015**, *347*, 970. (c) Kumar, P.; Thakur, U. K.; Alam, K.; Kar, P.; Kisslinger, R.; Zeng, S.; Patel, S.; Shankar, K. *Carbon* **2018**, *137*, 174−187.

(8) Wen, J.; Xie, J.; Chen, X.; Li, X. *Appl. Surf. Sci.* **2017**, *391*, 72−123.

(9) (a) Zhou, Z.; Zhang, Y.; Shen, Y.; Liu, S.; Zhang, Y. *Chem. Soc. Rev.* **2018**, *47*, 2298−2321. (b) Ong, W.-J.; Tan, L.-L.; Ng, Y. H.; Yong, S.-T.; Chai, S.-P. *Chem. Rev.* **2016**, *116*, 7159−7329. (c) Zheng, Y.; Lin, L.; Wang, B.; Wang, X. *Angew. Chem., Int. Ed.* **2015**, *54*, 12868−12884.

(10) (a) Cao, S.; Low, J.; Yu, J.; Jaroniec, M. *Adv. Mater.* **2015**, *27*, 2150−2176. (b) Wang, Y.; Wang, X.; Antonietti, M. *Angew. Chem., Int. Ed.* **2012**, *51*, 68−89. (c) Wang, Y.; Zhang, J.; Wang, X.; Antonietti, M.; Li, H. *Angew. Chem., Int. Ed.* **2010**, *49*, 3356−3359.

(11) (a) Zhang, Y.; Mori, T.; Ye, J.; Antonietti, M. *J. Am. Chem. Soc.* **2010**, *132*, 6294−6295. (b) Hong, J.; Xia, X.; Wang, Y.; Xu, R. *J. Mater. Chem.* **2012**, *22*, 15006−15012. (c) Wang, Y.; Di, Y.; Antonietti, M.; Li, H.; Chen, X.; Wang, X. *Chem. Mater.* **2010**, *22*, 5119−5121. (d) Ran, J.; Ma, T. Y.; Gao, G.; Du, X.-W.; Qiao, S. Z. *Energy Environ. Sci.* **2015**, *8*, 3708−3717. (e) Lin, J.; Pan, Z.; Wang, X. *ACS Sustainable Chem. Eng.* **2014**, *2*, 353−358. (f) Wang, Y.; Li, H.; Yao, J.; Wang, X.; Antonietti, M. *Chem. Sci.* **2011**, *2*, 446−450.

(12) (a) Yang, S.; Gong, Y.; Zhang, J.; Zhan, L.; Ma, L.; Fang, Z.; Vajtai, R.; Wang, X.; Ajayan, P. M. *Adv. Mater.* **2013**, *25*, 2452−2456. (b) Kumar, A.; Kumar, P.; Joshi, C.; Ponnada, S.; Pathak, A. K.; Ali, A.; Sreedhar, B.; Jain, S. L. *Green Chem.* **2016**, *18*, 2514−2521. (c) Kumar, A.; Kumar, P.; Pathak, A. K.; Chokkapu, A. N.; Jain, S. L. *ChemistrySelect* **2017**, *2*, 3437−3443.

(13) Mane, G. P.; Talapaneni, S. N.; Lakhi, K. S.; Ilbeygi, H.; Ravon, U.; Al-Bahily, K.; Mori, T.; Park, D. H.; Vinu, A. *Angew. Chem., Int. Ed.* **2017**, *56*, 8481−8485.

(14) (a) Mane, G. P.; Dhawale, D. S.; Anand, C.; Ariga, K.; Ji, Q.; Wahab, M. A.; Mori, T.; Vinu, A. *J. Mater. Chem. A* **2013**, *1*, 2913−2920. (b) Talapaneni, S. N.; Mane, G. P.; Park, D.-H.; Lakhi, K. S.; Ramadass, K.; Joseph, S.; Skinner, W. M.; Ravon, U.; Al-Bahily, K.; Vinu, A. *J. Mater. Chem. A* **2017**, *5*, 18183−18192. (c) Talapaneni, S. N.; Mane, G. P.; Mano, A.; Anand, C.; Dhawale, D. S.; Mori, T.; Vinu, A. *ChemSusChem* **2012**, *5*, 700−708. (d) Lakhi, K. S.; Park, D.-H.; Al-Bahily, K.; Cha, W.; Viswanathan, B.; Choy, J.-H.; Vinu, A. *Chem. Soc. Rev.* **2017**, *46*, 72−101.

(15) Kim, I. Y.; Kim, S.; Jin, X.; Premkumar, S.; Chandra, G.; Lee, N.-S.; Mane, G. P.; Hwang, S.-J.; Umapathy, S.; Vinu, A. *Angew. Chem.* **2018**, *130*, 17381−17386.

(16) Fang, J.; Fan, H.; Li, M.; Long, C. *J. Mater. Chem. A* **2015**, *3*, 13819−13826.

(17) Zhang, P.; Li, X.; Shao, C.; Liu, Y. *J. Mater. Chem. A* **2015**, *3*, 3281−3284.

(18) (a) Jürgens, B.; Irran, E.; Senker, J.; Kroll, P.; Müller, H.; Schnick, W. *J. Am. Chem. Soc.* **2003**, *125*, 10288−10300. (b) Chu, S.; Wang, C.; Feng, J.; Wang, Y.; Zou, Z. *Int. J. Hydrogen Energy* **2014**, *39*, 13519−13526. (c) Saplinova, T.; Lehnert, C.; Böhme, U.; Wagler, J.; Kroke, E. *New J. Chem.* **2010**, *34*, 1893−1908. (d) Chu, S.; Wang, Y.; Guo, Y.; Feng, J.; Wang, C.; Luo, W.; Fan, X.; Zou, Z. *ACS Catal.* **2013**, *3*, 912−919.

(19) Shiraishi, Y.; Kanazawa, S.; Kofuji, Y.; Sakamoto, H.; Ichikawa, S.; Tanaka, S.; Hirai, T. *Angew. Chem., Int. Ed.* **2014**, *53*, 13454−13459.

(20) Che, W.; Cheng, W.; Yao, T.; Tang, F.; Liu, W.; Su, H.; Huang, Y.; Liu, Q.; Liu, J.; Hu, F.; et al. *J. Am. Chem. Soc.* **2017**, *139*, 3021−3026.

(21) (a) Miller, D. R.; Swenson, D. C.; Gillan, E. G. *J. Am. Chem. Soc.* **2004**, *126*, 5372−5373. (b) Miller, D. R.; Holst, J. R.; Gillan, E. G. *Inorg. Chem.* **2007**, *46*, 2767−2774.

(22) Gillan, E. G. *Chem. Mater.* **2000**, *12*, 3906−3912.

(23) (a) Saplinova, T.; Bakumov, V.; Gmeiner, T.; Wagler, J.; Schwarz, M.; Kroke, E. *Z. Z. Anorg. Allg. Chem.* **2009**, *635*, 2480−2487. (b) Sattler, A.; Schönberger, S.; Schnick, W. *Z. Z. Anorg. Allg. Chem.* **2010**, *636*, 476−482.

(24) Makowski, S. J.; Köstler, P.; Schnick, W. *Chem. - Eur. J.* **2012**, *18*, 3248−3257.

(25) (a) Kumar, A.; Kumar, P.; Borkar, R.; Bansiwal, A.; Labhsetwar, N.; Jain, S. L. *Carbon* **2017**, *123*, 371−379. (b) Yu, H.; Shi, R.; Zhao, Y.; Bian, T.; Zhao, Y.; Zhou, C.; Waterhouse, G. I.; Wu, L. Z.; Tung, C. H.; Zhang, T. *Adv. Mater.* **2017**, *29*, 1605148.

(26) (a) Xia, P.; Zhu, B.; Yu, J.; Cao, S.; Jaroniec, M. *J. Mater. Chem. A* **2017**, *5*, 3230−3238. (b) Mao, J.; Peng, T.; Zhang, X.; Li, K.; Ye, L.; Zan, L. *Catal. Sci. Technol.* **2013**, *3*, 1253−1260.

(27) Axen, N.; Botton, G.; Somekh, R.; Hutchings, I. *Diamond Relat. Mater.* **1996**, *5*, 163−168.

(28) Hu, J.; Yang, P.; Lieber, C. M. *Phys. Rev. B: Condens. Matter Mater. Phys.* **1998**, *57*, R3185.

(29) Li, X.; Zhang, J.; Shen, L.; Ma, Y.; Lei, W.; Cui, Q.; Zou, G. *Appl. Phys. A: Mater. Sci. Process.* **2009**, *94*, 387−392.

(30) Seyfarth, L.; Senker, J. *Phys. Chem. Chem. Phys.* **2009**, *11*, 3522−3531.

(31) (a) Sehnert, J.; Baerwinkel, K.; Senker, J. *J. Phys. Chem. B* **2007**, *111*, 10671−10680. (b) Hu, Y.; Shim, Y.; Oh, J.; Park, S.; Park, S.; Ishii, Y. *Chem. Mater.* **2017**, *29*, 5080−5089.

(32) Cui, Y.; Ding, Z.; Fu, X.; Wang, X. *Angew. Chem., Int. Ed.* **2012**, *51*, 11814−11818.

(33) Sattler, A.; Pagano, S.; Zeuner, M.; Zurawski, A.; Gunzelmann, D.; Senker, J.; Müller-Buschbaum, K.; Schnick, W. *Chem. - Eur. J.* **2009**, *15*, 13161−13170.

(34) (a) Hsu, C.-Y.; Chang, K.-S. *J. Phys. Chem. C* **2018**, *122*, 3506−3512. (b) Rovnyak, D.; Baldus, M.; Itin, B. A.; Bennati, M.; Stevens, A.; Griffin, R. G. *J. Phys. Chem. B* **2000**, *104*, 9817−9822.

(35) Lotsch, B. V.; Schnick, W. *Chem. - Eur. J.* **2007**, *13*, 4956−4968.

(36) Guo, Q.; Zhang, Y.; Qiu, J.; Dong, G. *J. Mater. Chem. C* **2016**, *4*, 6839−6847.

(37) (a) Gulaczyk, I.; Kręglewski, M.; Valentin, A. *J. Mol. Spectrosc.* **2003**, *220*, 132−136. (b) Dirtu, D.; Odochian, L.; Pui, A.; Humelnicu, I. *Open Chem.* **2006**, *4*, 666−673.

(38) (a) Niu, P.; Zhang, L.; Liu, G.; Cheng, H. M. *Adv. Funct. Mater.* **2012**, *22*, 4763−4770. (b) Xu, J.; Zhang, L.; Shi, R.; Zhu, Y. *J. Mater. Chem. A* **2013**, *1*, 14766−14772.

(39) (a) Zheng, H.; Chen, W.; Gao, H.; Wang, Y.; Guo, H.; Guo, S.; Tang, Z.; Zhang, J. *J. Mater. Chem. C* **2017**, *5*, 10746−10753. (b) Lau, V. W.-h.; Mesch, M. B.; Duppel, V.; Blum, V.; Senker, J. r.; Lotsch, B. V. *J. Am. Chem. Soc.* **2015**, *137*, 1064−1072.

(40) (a) Wang, X.; Maeda, K.; Thomas, A.; Takanabe, K.; Xin, G.; Carlsson, J. M.; Domen, K.; Antonietti, M. *Nat. Mater.* **2009**, *8*, 76. (b) Bojdys, M. J.; Müller, J. O.; Antonietti, M.; Thomas, A. *Chem. - Eur. J.* **2008**, *14*, 8177−8182.

(41) Kroke, E.; Schwarz, M.; Horath-Bordon, E.; Kroll, P.; Noll, B.; Norman, A. D. *New J. Chem.* **2002**, *26*, 508−512.

(42) Tonda, S.; Kumar, S.; Kandula, S.; Shanker, V. *J. Mater. Chem. A* **2014**, *2*, 6772−6780.

(43) Jiang, J.; Ou-yang, L.; Zhu, L.; Zheng, A.; Zou, J.; Yi, X.; Tang, H. *Carbon* **2014**, *80*, 213−221.

(44) Cui, Y.; Zhang, J.; Zhang, G.; Huang, J.; Liu, P.; Antonietti, M.; Wang, X. *J. Mater. Chem.* **2011**, *21*, 13032−13039.

(45) Zhang, J.; Zhang, M.; Lin, S.; Fu, X.; Wang, X. *J. Catal.* **2014**, *310*, 24−30.

(46) (a) Sharma, P.; Sasson, Y. *Green Chem.* **2017**, *19*, 844−852. (b) Yuan, B.; Chu, Z.; Li, G.; Jiang, Z.; Hu, T.; Wang, Q.; Wang, C. *J. Mater. Chem. C* **2014**, *2*, 8212−8215.

(47) Zhang, G.; Zhang, M.; Ye, X.; Qiu, X.; Lin, S.; Wang, X. *Adv. Mater.* **2014**, *26*, 805−809.

(48) (a) Shalom, M.; Inal, S.; Fettkenhauer, C.; Neher, D.; Antonietti, M. *J. Am. Chem. Soc.* **2013**, *135*, 7118−7121. (b) Shalom, M.; Guttentag, M.; Fettkenhauer, C.; Inal, S.; Neher, D.; Llobet, A.; Antonietti, M. *Chem. Mater.* **2014**, *26*, 5812−5818.

(49) (a) Kang, Y.; Yang, Y.; Yin, L. C.; Kang, X.; Wang, L.; Liu, G.; Cheng, H. M. *Adv. Mater.* **2016**, *28*, 6471−6477. (b) Yang, P.; Ou, H.; Fang, Y.; Wang, X. *Angew. Chem., Int. Ed.* **2017**, *56*, 3992−3996.

(50) Alibart, F.; Lejeune, M.; Durand Drouhin, O.; Zellama, K.; Benlahsen, M. *J. Appl. Phys.* **2010**, *108*, No. 053504.

(51) (a) Zhang, Y.; Pan, Q.; Chai, G.; Liang, M.; Dong, G.; Zhang, Q.; Qiu, J. *Sci. Rep.* **2013**, *3*, 1943. (b) Sun, C.; Tay, B.; Lau, S.; Sun, X.; Zeng, X.; Li, S.; Bai, H.; Liu, H.; Liu, Z.; Jiang, E. *J. Appl. Phys.* **2001**, *90*, 2615−2617.

(52) Niu, P.; Liu, G.; Cheng, H.-M. *J. Phys. Chem. C* **2012**, *116*, 11013−11018.

(53) (a) Chen, L. C.; Teng, C. Y.; Lin, C. Y.; Chang, H. Y.; Chen, S. J.; Teng, H. *Adv. Energy Mater.* **2016**, *6*, 1600719. (b) Yeh, T. F.; Teng, C. Y.; Chen, S. J.; Teng, H. *Adv. Mater.* **2014**, *26*, 3297−3303. (c) Yeh, T.-F.; Chen, S.-J.; Yeh, C.-S.; Teng, H. *J. Phys. Chem. C* **2013**, *117*, 6516−6524. (d) Shi, R.; Li, Z.; Yu, H.; Shang, L.; Zhou, C.; Waterhouse, G. I.; Wu, L. Z.; Zhang, T. *ChemSusChem* **2017**, *10*, 4650−4656. (e) Chen, L. C.; Teng, C. Y.; Lin, C. Y.; Chang, H. Y.; Chen, S. J.; Teng, H. *Adv. Energy Mater.* **2016**, *6*, 1600719. (f) Shi, R.; Li, Z.; Yu, H.; Shang, L.; Zhou, C.; Waterhouse, G. I. N.; Wu, L.-Z.; Zhang, T. *ChemSusChem* **2017**, *10*, 4650−4656.

(54) Liang, Q.; Li, Z.; Huang, Z. H.; Kang, F.; Yang, Q. H. *Adv. Funct. Mater.* **2015**, *25*, 6885−6892.

(55) (a) Sun, J.; Zhang, J.; Zhang, M.; Antonietti, M.; Fu, X.; Wang, X. *Nat. Commun.* **2012**, *3*, 1139. (b) Liu, Q.; Chen, T.; Guo, Y.; Zhang, Z.; Fang, X. *Appl. Catal., B* **2016**, *193*, 248−258. (c) Ye, X.; Cui, Y.; Wang, X. *ChemSusChem* **2014**, *7*, 738−742.

(56) (a) Chen, Z.; Sun, P.; Fan, B.; Liu, Q.; Zhang, Z.; Fang, X. *Appl. Catal., B* **2015**, *170*, 10−16. (b) Zhang, M.; Duan, Y.; Jia, H.; Wang, F.; Wang, L.; Su, Z.; Wang, C. *Catal. Sci. Technol.* **2017**, *7*, 452−458.

(57) (a) Qin, J.; Wang, S.; Ren, H.; Hou, Y.; Wang, X. *Appl. Catal., B* **2015**, *179*, 1−8. (b) Luo, L.; Zhang, M.; Wang, P.; Wang, Y.; Wang, F. *New J. Chem.* **2018**, *42*, 1087−1091.

(58) Ali, H. *Water, Air, Soil Pollut.* **2010**, *213*, 251−273.

(59) Mittal, A.; Mittal, J.; Malviya, A.; Kaur, D.; Gupta, V. *J. Colloid Interface Sci.* **2010**, *343*, 463−473.

(60) Yagub, M. T.; Sen, T. K.; Afroze, S.; Ang, H. M. *Adv. Colloid Interface Sci.* **2014**, *209*, 172−184.

(61) (a) Fronczak, M.; Krajewska, M.; Demby, K.; Bystrzejewski, M. *J. Phys. Chem. C* **2017**, *121*, 15756−15766. (b) Zhu, B.; Xia, P.; Ho, W.; Yu, J. *Appl. Surf. Sci.* **2015**, *344*, 188−195.

(62) Langmuir, I. *J. Am. Chem. Soc.* **1918**, *40*, 1361−1403.

(63) Freundlich, H. *J. Phys. Chem.* **1906**, *57*, 1100−1107.

(64) Han, S.; Liu, K.; Hu, L.; Teng, F.; Yu, P.; Zhu, Y. *Sci. Rep.* **2017**, *7*, 43599.

(65) Gaya, U. I.; Abdullah, A. H. *J. Photochem. Photobiol., C* **2008**, *9*, 1−12.

(66) Ahmad, H.; Kamarudin, S.; Minggu, L.; Kassim, M. *Renewable Sustainable Energy Rev.* **2015**, *43*, 599−610.

(67) Pelaez, M.; Nolan, N. T.; Pillai, S. C.; Seery, M. K.; Falaras, P.; Kontos, A. G.; Dunlop, P. S.; Hamilton, J. W.; Byrne, J. A.; O'shea, K.; et al. *Appl. Catal., B* **2012**, *125*, 331−349.

(68) Zhou, X.; Peng, F.; Wang, H.; Yu, H.; Fang, Y. *Chem. Commun.* **2011**, *47*, 10323−10325.

(69) (a) Zheng, X. J.; Chen, B.; Yang, M. J.; Wu, C. C.; Orler, B.; Moore, R. B.; Zhu, K.; Priya, S. *ACS Energy Lett.* **2016**, *1*, 424−430. (b) Askar, A. M.; Bernard, G. M.; Wiltshire, B.; Shankar, K.; Michaelis, V. K. *J. Phys. Chem. C* **2017**, *121*, 1013−1024.

(70) Zhao, Y.; Nardes, A. M.; Zhu, K. *Faraday Discuss.* **2014**, *176*, 301−312.

(71) Wu, C. G.; Chiang, C. H.; Chang, S. H. *Nanoscale* **2016**, *8*, 4077−4085.

(72) Li, Z.; Boix, P. P.; Xing, G. C.; Fu, K. W.; Kulkarni, S. A.; Batabyal, S. K.; Xu, W. J.; Cao, A. Y.; Sum, T. C.; Mathews, N.; Wong, L. H. *Nanoscale* **2016**, *8*, 6352−6360.

(73) Zuo, C. T.; Ding, L. M. *Adv. Energy Mater.* **2017**, *7*, 1601193.

(74) Liang, Y. Q.; Wang, Y. J.; Mu, C.; Wang, S.; Wang, X. N.; Xu, D. S.; Sun, L. C. *Adv. Energy Mater.* **2018**, *8*, 1701159.

(75) Sheng, R.; Ho-Baillie, A.; Huang, S. J.; Chen, S.; Wen, X. M.; Hao, X. J.; Green, M. A. *J. Phys. Chem. C* **2015**, *119*, 3545−3549.

(76) Ryu, S.; Noh, J. H.; Jeon, N. J.; Kim, Y. C.; Yang, S.; Seo, J. W.; Seok, S. I. *Energy Environ. Sci.* **2014**, *7*, 2614−2618.

(77) (a) Chen, X.; Liu, Q.; Wu, Q.; Du, P.; Zhu, J.; Dai, S.; Yang, S. *Adv. Funct. Mater.* **2016**, *26*, 1719−1728. (b) He, M.; Chen, Y.; Liu, H.; Wang, J.; Fang, X.; Liang, Z. *Chem. Commun.* **2015**, *51*, 9659−9661. (c) Zhu, Z.; Ma, J.; Wang, Z.; Mu, C.; Fan, Z.; Du, L.; Bai, Y.; Fan, L.; Yan, H.; Phillips, D. L.; et al. *J. Am. Chem. Soc.* **2014**, *136*, 3760−3763. (d) Hadadian, M.; Correa-Baena, J. P.; Goharshadi, E. K.; Ummadisingu, A.; Seo, J. Y.; Luo, J.; Gholipour, S.; Zakeeruddin, S. M.; Saliba, M.; Abate, A.; et al. *Adv. Mater.* **2016**, *28*, 8681−8686. (e) Jiang, L. L.; Wang, Z. K.; Li, M.; Zhang, C. C.; Ye, Q. Q.; Hu, K. H.; Lu, D. Z.; Fang, P. F.; Liao, L. S. *Adv. Funct. Mater.* **2018**, *28*, 1705875.

(78) (a) Kirchartz, T.; Gong, W.; Hawks, S. A.; Agostinelli, T.; MacKenzie, R. C. I.; Yang, Y.; Nelson, J. *J. Phys. Chem. C* **2012**, *116*, 7672−7680. (b) Guo, X.; Tan, Q.; Liu, S.; Qin, D.; Mo, Y.; Hou, L.; Liu, A.; Wu, H.; Ma, Y. *Nano Energy* **2018**, *46*, 150−157. (c) Liu, Z.; Zhu, A.; Cai, F.; Tao, L.; Zhou, Y.; Zhao, Z.; Chen, Q.; Cheng, Y.-B.; Zhou, H. *J. Mater. Chem. A* **2017**, *5*, 6597−6605. (d) Liu, Z.; Chang, J.; Lin, Z.; Zhou, L.; Yang, Z.; Chen, D.; Zhang, C.; Liu, S.; Hao, Y. *Adv. Energy Mater.* **2018**, *8*, 1703432. (e) Jahandar, M.; Heo, J. H.; Song, C. E.; Kong, K.-J.; Shin, W. S.; Lee, J.-C.; Im, S. H.; Moon, S.-J. *Nano Energy* **2016**, *27*, 330−339. (f) He, Q.; Yao, K.; Wang, X.; Xia, X.; Leng, S.; Li, F. *ACS Appl. Mater. Interfaces* **2017**, *9*, 41887−41897. (g) Niu, G.; Wang, S.; Li, J.; Li, W.; Wang, L. *J. Mater. Chem. A* **2018**, *6*, 4721−4728.

(79) (a) Lin, W.; Cao, E.; Zhang, L.; Xu, X.; Song, Y.; Liang, W.; Sun, M. *Nanoscale* **2018**, *10*, 5482−5488. (b) Kang, L.; Chu, J.; Zhao, H.; Xu, P.; Sun, M. *J. Mater. Chem. C* **2015**, *3*, 9024−9037. (c) Ding, Q.; Shi, Y.; Chen, M.; Li, H.; Yang, X.; Qu, Y.; Liang, W.; Sun, M. *Sci. Rep.* **2016**, *6*, 32724. (d) Wu, H. Y.; Lai, Y. H.; Hsieh, M. S.; Lin, S. D.; Li, Y. C.; Lin, T. W. *Adv. Mater. Interfaces* **2014**, *1*, 1400119.

(80) (a) Liang, X.; You, T.; Liu, D.; Lang, X.; Tan, E.; Shi, J.; Yin, P.; Guo, L. *Phys. Chem. Chem. Phys.* **2015**, *17*, 10176−10181. (b) Zhao, J.; Sun, M.; Liu, Z.; Quan, B.; Gu, C.; Li, J. *Sci. Rep.* **2015**, *5*, 16019.

(81) Siekkinen, A. R.; McLellan, J. M.; Chen, J.; Xia, Y. *Chem. Phys. Lett.* **2006**, *432*, 491−496.

(82) Dong, B.; Fang, Y.; Xia, L.; Xu, H.; Sun, M. *J. Raman Spectrosc.* **2011**, *42*, 1205−1206.

(83) (a) Canpean, V.; Iosin, M.; Astilean, S. *Chem. Phys. Lett.* **2010**, *500*, 277−282. (b) Fang, Y.; Li, Y.; Xu, H.; Sun, M. *Langmuir* **2010**, *26*, 7737−7746.

(84) (a) Kang, Y.; Yang, Y.; Yin, L. C.; Kang, X.; Liu, G.; Cheng, H. M. *Adv. Mater.* **2015**, *27*, 4572−4577. (b) Niu, P.; Qiao, M.; Li, Y.; Huang, L.; Zhai, T. *Nano Energy* **2018**, *44*, 73−81.

(85) (a) Dang, Q.-Q.; Wang, X.-M.; Zhan, Y.-F.; Zhang, X.-M. *Polym. Chem.* **2016**, *7*, 643−647. (b) Patel, H. A.; Je, S. H.; Park, J.; Chen, D. P.; Jung, Y.; Yavuz, C. T.; Coskun, A. *Nat. Commun.* **2013**, *4*, 1357. (c) Patel, H. A.; Je, S. H.; Park, J.; Jung, Y.; Coskun, A.; Yavuz, C. T. *Chem. - Eur. J.* **2014**, *20*, 772−780.

(86) (a) Clark, M. *Handbook of textile and industrial dyeing: principles, processes and types of dyes*; Elsevier: 2011. (b) Zollinger, H. *Color chemistry: syntheses, properties, and applications of organic dyes and pigments*; John Wiley & Sons: 2003. (c) Robin, M. B.; Simpson, W. T. J. *J. Chem. Phys.* **1962**, *36*, 580−588.